Fracture response of X65 pipes containing circumferential flaws in the presence of Lüders plateau

Longjie Wang[a, b], Guiyi Wu[c], Bin Wang[b], Henryk Pisarski[d]

[a] National Structural Integrity Research Centre, Granta Park, Cambridge, CB21 6AL, United Kingdom

[b] College of Engineering, Design and Physical Sciences, Brunel University London, Kingston Lane, Uxbridge, Middlesex, UB8 3PH, United Kingdom

[c] Integrity Management Group, TWI Ltd, Granta Park, Cambridge, CB21 6AL, United Kingdom

[d] Structural integrity consultant

Nomenclature

h	stress triaxiality
2c	crack length
α	dimensionless constant in Ramberg-Osgood model
Δa_n	crack extension
Δe_L	strain extent of Lüders plateau, known as Lüders strain
δ	crack tip opening displacement
Δs	difference between s_U and s_L
ρ_0	initial radius of the blunt crack tip
σ	true stress
σ_0	reference stress in Ramberg-Osgood model
$\sigma_{0.2}$	0.2% proof stress on the true stress-true strain curve
σ_h	hydrostatic stress
σ_{ij}	stress components of the stress field at crack tip
θ	angular position ahead of crack tip
σ_{ij}	function of strain hardening exponent n and angular position θ at crack tip
ε	true strain

ε_0	reference strain in Ramberg-Osgood model
ε_{eq}^{p}	equivalent plastic strain
a	crack depth
a_0	initial crack depth
E	Young's modulus
e	engineering strain
E_L	softening modulus of the softening segment in UDU stress-strain model
$\overline{E}_L$	normalised softening modulus
$e_{0,avg}$	average overall strain
I_n	constant depending on n
J	the J-integral
L	half-length of the pipe, also the length of the quarter FE pipe model
m	J-δ constant that depends on the strain hardening exponent and the geometry of cracked component
N	coefficient of the power-law strain rate-dependence law
r	radial distance from crack tip

R_{eL}	lower yield stress or the plateau stress of the measured engineering stress-strain curve
s	engineering stress or gross stress of the flawed pipe
s_{ly}	lower yield stress of the UDU stress-strain model in the engineering stress-strain form
s_{uy}	upper yield stress of the UDU stress-strain model in the engineering stress-strain form
t	pipe wall thickness
API	American Petroleum Association
BS	British Standard
CRES	Center for Reliable Energy Systems
CTOD	crack tip opening displacement
DIC	digital image correlation
DNV	Det Norske Veritas
ECA	engineering critical assessment
EDM	electric discharge machining
FE	finite element
HRR	Hutchinson-Rice-Rosengren

LVDT	linear variable differential transducer
OD	outer diameter of the pipe
RO	Ramberg-Osgood
SB-ECA	strain-based engineering critical assessment
SBD	strain-based design
SINTEF	Stiftelsen for industriell og teknisk forskning, meaning The Foundation for Scientific and Industrial Research
UDU	up-down-up

Abstract

A yield discontinuity or Lüders plateau can be observed in tensile tests conducted on seamless pipe manufactured to API 5L X65 strength grade steel. Such material behaviour is associated with strain localisation which can significantly affect the fracture behaviour of X65 steel pipe subjected to plastic strain. This study considers the Lüders plateau, using the so-called "up-down-up" (UDU) constitutive model, in finite element (FE) analyses of seamless X65 pipes containing circumferential surface-breaking cracks and subjected to axial plastic straining. The softening modulus of UDU model was found to significantly affect the simulated evolution of plasticity, crack driving force and crack-tip fields of the cracked pipe. The FE analysis results were validated against the full-scale pipe test data. It was found that by correctly selecting the softening modulus, a suitable level of accuracy and conservatism was obtained by using an UDU model in FE analyses for assessing fracture response of flawed pipes which show Lüders plateau behaviour. In contrast, the existing stress- and strain-based fracture assessment solutions generally underestimate the crack driving force in the Lüders plateau phase.

Keywords: fracture, Lüders plateau, localised band, finite element analysis, strain-based

Highlights

- The UDU models are demonstrated to be able to capture Lüders plateau propagation along the pipe axis in the FE modelling of a cracked pipe.
- The softening moduli of the UDU models are found to significantly affect the simulated Lüders plateau propagation, crack-tip field, and thus the crack driving force of a cracked pipe.
- The conventional treatment of a material stress-strain curve with Lüders plateau is unable to realistically capture the Lüders plateau propagation along the pipe and may result in non-conservatism in a fracture assessment of cracked pipes.
- The crack driving force estimated using the correct UDU model, with consideration of ductile tearing, is demonstrated to best represent that measured in the large-scale tests of an X65 cracked pipe with Lüders plateau and subjected to axial plastic straining.

1. Introduction

Pipelines are cost-effective and efficient tools for transporting oil and gas. Because of ever-increasing energy demands, more pipelines are being designed and constructed to operate in harsh and remote environments, which include seismically-active and permafrost regions. The pipelines operating in these environments are potentially subjected to large plastic deformations, posing threats to the pipeline integrity. Furthermore, pipeline installation methods, such reeling, will impose plastic straining during installation. Strain-based design (SBD) techniques allow the pipelines to withstand a certain amount of plastic deformation during installation and operation conditions. The significance of crack-like flaws that might be present in the pipeline girth welds subjected to plastic straining are assessed using strain-based engineering critical assessment (SB-ECA) methods. These methods are based on fracture mechanics principles. Seamless steel pipe to API 5L X65 strength grade is often hot-finished during fabrication, which may result in yield discontinuity known as Lüders plateau. In a uni-axial tensile test, a pronounced yield point followed by a stress drop and then a nearly constant stress plateau followed by a rising stress-strain curve is usually observed.

Lüders plateau, first reported by Piobert et al. (1842) and Lüders (1860), is a material instability frequently encountered in mild steels. This material characteristic was shown to be the result of dislocation pinning (Cottrell and Bilby, 1949) accounting for the upper yield stress, and dislocation release and multiplication (Johnston and Gilman, 1959) leading to the subsequent stress drop. The Lüders plateau is manifest by the propagation of localised deformation bands (Lüders bands) during uni-axial tensile tests. Fig. 1 shows a typical stress-strain curve of an API X65 steel displaying Lüders plateau with a Lüders strain Δe_L of about 2% (Wang et al., 2017). The numbered bullet points correspond to the in-plane deformation contours measured by digital image correlation (DIC). The localisation band usually initiates at stress concentrators (e.g. in this case the shoulder of a tensile specimen).and then propagates at an inclination angle of approximately 55°. Previous studies (e.g. Aguirre et al., 2004; Kyriakides et al., 2008; Hallai and Kyriakides, 2011; Liu et al., 2015) have shown that the Lüders plateau has significant effect on the structural behaviour and deformation capacity of steel. Thus, a consideration of the effect of Lüders plateau in engineering applications is required.

In current codified engineering critical assessment (ECA) procedures such as BS7910 (2015), DNV-RP-F108 (2006) and R6 Rev.4 (2001), the behaviour of materials exhibiting Lüders is treated as a stress-strain curve containing a flat stress plateau (i.e. straining at constant stress) which bridges the linear-elastic and the strain hardening branches; the upper yield stress is ignored. This type of stress-strain curve has been used in other studies (Tang et al., 2014; Tkaczyk et al., 2009; Pisarski et al., 2014) in which the steel exhibits a Lüders plateau. Wang et al. (2017) showed that this type of stress-strain curve failed to reproduce the macroscopic features of the Lüders band observed in experiments on tensile specimens and full-scale pipe tests. They found that finite element (FE) analysis using this stress-strain curve predicted a non-conservative CTOD crack driving force in comparison with the full-scale test results. In the present study, we investigated the influence of the constitutive models on the crack driving force and the structural behaviour of the cracked pipes. We have demonstrated that the effect of Lüders plateau in fracture analysis of cracked pipes can be appropriately evaluated by the correct “up-down-up” (UDU) constitutive model.

2. Finite element model of pipes containing flaws

FE models were created in accordance with the geometry and configuration of the full-scale tests carried out at TWI and reported by Pisarski et al. (2014). Both uni-axially and bi-axially loaded pipe tests were conducted in the full-scale test programme. In this paper, we focus on the analysis of the uni-axially loaded pipe test. The seamless steel pipe had a length (2*L*) of 2000 mm, an outer diameter (OD) of 273.3 mm and an average wall thickness (*t*) of 18.4 mm. The pipe contained four canoe-shaped notches that were manufactured using electric discharge machining (EDM). Each notch has a finite radius of 0.12 mm at the notch tip. The four notches were at the cardinal points around the pipe circumference, namely the 0, 3, 6 and 12 o'clock positions. The notches at the opposite positions had identical in sizes. We report the simulation of both the notches at 3 and 9 o'clock each with a nominal size of 6×50 mm, and that at 6 and 12 o'clock each with a nominal size of 5×100 mm. In favour of brevity, the detailed analysis of the Lüders banding behaviour and the crack-tip field was reported for the 6×50 mm notch only since the effect of the material model on these features exhibit similar trend.

To accurately simulate the crack behaviour, we used the actual notch sizes in the FE analyses; these had average sizes of 5.68×50 mm (a/t = 0.31, $\emptyset/\pi$ = 0.058), and 4.41×100 mm (a/t = 0.24, $\emptyset/\pi$ = 0.116), respectively. Fig. 2 shows the crack configuration and pipe geometry.

2.1 Constitutive model

The constitutive model used in this study is the so-called UDU stress-strain response. The model is an isotropic, J_2 type, elastic-plastic material law assuming incremental plasticity, and contains a segment of strain softening followed by conventional strain hardening. To the best knowledge of the authors, Kyriakides and Miller (2000) were among the first to use the UDU model to simulate strain localisation due to Lüders phenomenon in FE analysis. The UDU is a simplified approach used to fit to the experimentally determined engineering stress-strain curve that contains a Lüders plateau. Fig. 3 illustrates how the UDU fit is constructed. The fit consists of four branches, namely the linear-elastic, linear softening, linear hardening and the measured strain hardening branches. The fit is constructed such that the so-called Maxwell stress is equal to plateau stress (R_{eL}). Artificial upper and lower yield strengths are then created. A straight line joining these points creates two triangles above and below the Maxwell stress, as shown in Fig. 3. According to the Maxwell equal area rule, the area of the two triangles are made equal. This requirement is to ensure that the dissipated energy remains unchanged during the Lüders phase. Accordingly, the upper yield stress (s_{uy}) and the lower yield stress (s_{ly}) can be determined as:

$$s_{\mathrm{uy}} - R_{eL} = R_{eL} - s_{\mathrm{ly}} = \frac{\Delta s}{2} \tag{1}$$

where Δs is the difference between s_{uy} and s_{ly}. Δs is related to the softening modulus (E_L) by:

$$E_L = -\frac{\Delta s}{\Delta e_L} = -\frac{s_{\mathrm{uy}} - s_{\mathrm{ly}}}{\Delta e_L} \tag{2}$$

where Δe_L is the length of Lüders plateau in terms of engineering strain. The material properties of the cracked pipe analysed in this work refer to those presented in Pisarski et al. (2014). The pipe is seamless to API 5L Grade X65 steel that exhibited a marked Lüders plateau with strain extent (Δe_L) of about 2%. Fig. 4 shows the average engineering stress-strain curve of the X65 pipe, which ignored the upper yield strength that was observed in the tensile tests (Pisarski et al., 2014), with the UDU fit with different normalised softening modulus ($\bar{E}_L \equiv |E_L/E|$). The parameters of the constitutive models are shown in detail in Table 1.

2.2 FE model configuration

The FE pipe model was generated using the commercial FE software Abaqus 6.14. Only a quarter of the pipe (L=1000 mm) was simulated because of the application of symmetry boundary conditions. The model was discretized by the 20-node brick element with reduced integration (type C3D20R). Fig. 5 shows the typical mesh configuration used in this study, together with the associated boundary conditions. Nodal displacements were prescribed at the uncracked end such that an average overall strain $e_{o,avg}$ of about 0.06 was obtained. A bottom node was constrained to avoid the possible rigid body motion. The spider-web focused mesh using non-singular elements was applied to the crack tip. The mesh had 16 elements in a row along the half circumference. The bulk of the pipe was discretized with different mesh density for different constitutive models. The stress-strain curve (in its engineering form) containing a flat stress plateau (denoted as FLAT in this paper) is expected to produce generally uniform deformation in the FE analysis because the corresponding true stress-true strain response of the FLAT model has a monotonically increasing trend over the whole strain range. Therefore, a coarser mesh was used with a smooth mesh transition in which the longitudinal element length ranges from 10 to 200 mm. As for the UDU stress-strain response, a refined mesh was applied to the bulk of the pipe to capture the strain localisations due to Lüders plateau. The elements were applied through the pipe wall thickness with dimensions in other orientations (circumferential and longitudinal) being equal to those in the thickness direction. Such an isotropic mesh pattern was chosen to avoid potential directional bias of element arrangement. The mesh was derived from a mesh sensitivity study, which reproduced the Lüders banding pattern similar to that reported in literature (Aguirre et al., 2004; Kyriakides et al., 2008; Hallai and Kyriakides, 2011; Liu et al., 2015).

It is well-known that strain softening (or a negative tangent stiffness $\partial\Delta\sigma/\partial\Delta\varepsilon$) in the constitutive model can result in spurious mesh sensitivity of FE results. The reason is that strain softening renders the governing partial differential equations (PDEs) ill-defined and the ellipticity of the PDEs lost, leading to non-uniqueness of the solution. To remove the induced mesh sensitivity, a mild strain rate dependence was applied (Needleman, 1988). A simple power-law rate-dependence (Hallai and Kyriakides, 2011; Liu et al., 2015) was used, which takes the following form:

$$\left(\frac{\dot{\varepsilon}^p}{\dot{\varepsilon}_0^p}\right)^N = \frac{\sigma}{\sigma_0(\varepsilon^p)} \tag{3}$$

Where $\dot{\varepsilon}^p$ is the actual plastic strain rate, $\dot{\varepsilon}_0^p$ is the reference equivalent strain rate (assumed to be $10^{-4}s^{-1}$ in this work), $\sigma_0(\varepsilon^p)$ is stress corresponding to the applied plastic strain at the reference plastic strain rate, σ is the stress corresponding to the applied plastic strain at the actual plastic strain rate, and N is the exponent describing the strain rate dependence. In this work, N is taken as 0.001, which is deemed sufficient to reduce the mesh sensitivity while having marginal effect on the simulated behaviour. The strain rate-dependence was applied in Abaqus 6.14 via the yield ratio option.

A series of pipe models was generated to account for the effect of ductile tearing from the notches. This is described in section 2.3. Similar mesh strategy was used for other pipe models. The total element number of the refined mesh for analyses using UDU material model ranged from 69872 (326867 nodes) to 77764 (359850 nodes) depending on the specific crack dimensions.

The FE models were computed using an implicit time integration scheme and Newton-Raphson iteration. Geometric nonlinearity and finite strain formulation were incorporated. Crack tip opening displacement (CTOD), load-displacement response and average overall strain were extracted. The average overall strain ($e_{o,avg} = (e_{o,1} + e_{o,2})/2$) is defined as the mean value of the strain measured from virtual LVDT1 ($e_{o,1}$) and LVDT2 ($e_{o,2}$) located at the upper and lower edges of the pipe in Fig. 5, respectively. The CTOD was calculated by using the 90° intercept definition proposed by Rice (1968). It is known that in finite strain analysis, J-integral often exhibits noticeable path-dependence, invalidating its use as a fracture parameter. Brocks and Scheider (2001) demonstrated the J-integral at the outermost contours tend to converge and approach to the far-field J, and recommended to extract the J from the furthest contour which is not in contact with the model boundary. However, in the present study the J-integral was not adopted as crack driving force due to the spurious path-dependence even for the outermost contours. Fig. 6 shows the locations of the contours from which the J-integral were extracted. In total, 30 contours were defined such that the innermost contour (contour 1) being along the notch and the outmost contour (contour 30) being closest to but not in contact with the boundary of the model. Only a few contours were marked in Fig. 6 for illustration purpose. It can be noticed in Fig. 7 that the J curves from the outermost contours are initially well converged, and then start to diverge in the strain range $e_{o,avg}$ = 0.01-0.025. A pronounced decreasing trend in the J is also observed, which is expected to be due to the strain softening. Strain softening is believed to invalidate the use of J as the fundamental assumption of J was violated (Brocks and Scheider, 2001).

2.3 Consideration of ductile tearing

In the pipe tests reported in Pisarski et al. (2014), ductile tearing occurred during the test. Ductile tearing increases crack depth which leads to a higher crack driving force than that with the initial crack depth. However, this effect cannot be explicitly captured in the FE analysis of a stationary crack. In order to incorporate the effect of ductile tearing the driving force mapping approach (Hertelé Ghent et al., 2012, 2014) was adopted. The mapping approach requires a series of FE simulations to be conducted with crack depths ranging from the initial depth a_0 to a prescribed final depth $a_0 + \Delta a_n$. The predicted CTOD and crack extension can then be interpreted from the intersections of the crack growth resistance curve (R-curve) and a series of iso-strain CTOD curves. The iso-strain CTOD curves refer to a series of CTOD curves as a function of crack growth at a specified strain. The mapping approach has also been commonly used by researchers to predict crack extension and the strain capacity of pipeline girth welds (Fairchild et al., 2011, Pisarski et al., 2014).

In the present study, simulations of crack depth $a = 5.68, 6, 7, 8, 9$ for 6×50 mm notch mm were performed to incorporate the effect of ductile tearing.. Iso-strain CTOD curves were constructed for an average overall strain $e_{o,avg}$ increasing from 0 with an increment of 0.0005 until a tangency with the R-curve was reached. The CTOD R-curve (obtained from SENT tests) of the parent material was reported in Pisarski et al. (2014) as $\delta = 1.917\Delta a^{0.704}$. The iso-strain CTOD curves were established by applying fourth order curve fitting to the points (CTOD$_i$, a_i) for the discrete crack depths. For instance, two iso-strain CTOD curves for $e_{o,avg}$ = 0.03 and $e_{o,avg}$ = 0.0435 for 6×50 mm notch are shown in Fig. 8. The iso-strain CTOD curve for $e_{o,avg}$ = 0.03 intersects the SENT R-curve at the point (6.528, 1.708), indicating the crack depth of 6.528 mm and the corresponding CTOD of 1.708 mm. The ductile instability was deemed to occur when the tangency between the iso-strain CTOD curve (when $e_{o,avg}$ = 0.0435) and the R-curve was reached. Using the mapping approach, we have obtained a CTOD versus the average overall strain ($e_{o,avg}$) curve with the actual CTOD values incorporating the effect of ductile tearing, as shown in Fig. 8 (b).

3. Results

3.1 Global deformation response

The load-displacement or the gross stress-average overall strain (s-$e_{o,avg}$) response is a key indicator of the global behaviour of a deforming structure. The gross stress is defined as the remote stress applied at the end of the pipe, which is expressed as $s = F/A$ where F is the applied force and A is the cross-section area of the uncracked end. Fig. 9 shows the gross stress versus average overall strain response (s-$e_{O,avg}$). The s-$e_{O,avg}$ response was defined as the average of the overall strains $e_{O,1}$ (from virtual LVDT 1) and $e_{O,2}$ (from virtual LVDT 2). The s-$e_{O,avg}$ responses produced using different stress-strain models indicate similar trends and show a stress plateau followed by strain hardening. The FE model with FLAT stress-strain curve produced the lowest stress plateau of 512 MPa, which is 4.12% lower than the tested value. The height and length of the stress plateau is observed to increase with the increasing $\bar{E}_L$. This behaviour was also noted on pipes loaded in bending but without flaws by other researchers (Hallai and Kyriakides, 2011). All global stress versus strain curves converge in the strain hardening regime following the Lüders plateau phase.

Apart from the stress plateau, the $\bar{E}_L$ ratio additionally affects the yield point. As expected, the s-$e_{O,avg}$ curve calculated with the FLAT stress-strain model shows neither an upper yield point nor the subsequent stress drop. Similar behaviour is found for s-$e_{O,avg}$ response calculated with $\bar{E}_L = 0.005$ except that the stress slightly drops at about $e_{O,avg}$ = 0.008. On the other hand, the s-$e_{O,avg}$ responses for $\bar{E}_L = 0.015$ and $\bar{E}_L = 0.025$, have noticeable upper yield stresses of 531 MPa and 548 MPa, respectively

3.2 Evolution of plasticity

From the gross stress versus average overall strain (s-$e_{o,avg}$) curves, six configurations were selected for each stress-strain model to show the progression of plastic deformation. Fig. 10 shows the equivalent plastic strain (ε_{eq}^{p}) distributions on the deformed pipe for different overall strain levels.

Initially, when $e_{o,avg}$ = 0.002, the simulated pipe is globally elastic; shown in white colour covering the whole pipe. Limited plasticity is found to accumulate at the crack tip. At the onset of the elastic-plastic transition on the s-$e_{o,avg}$ curves, localised shear bands emanate from the crack tip in all models. The width of the localised band tends to be narrower for the UDU model with a higher E_L. This indicates that higher E_L leads to stronger strain localisation. Beyond $e_{o,avg}$ = 0.003, the plasticity starts to spread to the elastically strained parts of the pipe. When $\mathrm{e_{o,avg}}$ = 0.01, which is about one third of the stress plateau extent, prominent differences in the band patterns are observed. In the case using FLAT stress-strain curve, uniform plasticity is observed to spread over the pipe, indicating homogeneous deformation. In contrast, the FE models using UDU stress-strain curves exhibit inhomogeneous deformation, featuring propagating localised plastic band(s). It is worth noting that FE model using $\bar{E}_L = 0.005$ yields more complex bands initiating at different locations of the pipe simultaneously. When $\bar{E}_L =$ 0.015 and 0.025, localised bands are formed near the cracked region and propagate to the remaining parts of the pipe. When $e_{o,avg}$ = 0.02, the pipe model using the FLAT stress-strain curve continues to deform homogeneously. The models using UDU stress-strain curves still experience propagation of localised plastic bands towards the elastically strained parts of the pipes except in the model using $\bar{E}_L = 0.005$ where the band has covered the whole pipe. When

$e_{o,avg}$ = 0.027, the pipes simulated with $\bar{E}_L$ = 0.005 and 0.015 have entered the globally strain hardening regime in which the pipes deform uniformly. In the model simulated with $\bar{E}_L = 0.025$, the Lüders band propagates through a majority of the pipe, and starts to deform uniformly after $e_{o,avg}$ = 0.035. This indicates that the increase of $\bar{E}_L$ in UDU model will result in the increase of stress plateau extent which is shown in Fig. 9.

To examine in further detail the evolution of plasticity in the pipe, the equivalent plastic strain (ε_{eq}^{p}) profiles along two paths (path AB and A'B' as shown in Fig. 11) are plotted against the normalised distance (*x/L*) along the pipe axis in Fig. 12 and Fig. 13, respectively. Paths AB and A'B' represent the upper and lower edges of the pipe, respectively. Both paths are on the inner surface of the pipe. Fig. 12 and Fig. 13 show the respective ε_{eq}^{p} profiles on the path AB and path A'B' for different $e_{o,avg}$. levels. When $e_{o,avg}$ =0.002, little plasticity is observed as the pipe is globally elastic. When $e_{o,avg}$ = 0.003, prominent strain localisation associated with net section yielding occurring at the cracked end are observed in Fig. 12 and Fig. 13. More localised plasticity is produced with a greater $\bar{E}_L$, which is reflected by the narrower width of the strain peak (bump) produced along path AB and A'B' (Fig. 12 and Fig. 13) using greater $\bar{E}_L$ when $e_{o,avg} = 0.003$. It is also shown that the greater the $\bar{E}_L$, the higher the peak value of ε_{eq}^{p} except that using $\bar{E}_L = 0.025$ because the plasticity of model using this $\bar{E}_L$ value just reaches the bottom edge.

For $e_{o,avg}$ between 0.01 and 0.035, ε_{eq}^{p} for the FLAT stress-strain model remains nearly constant with the distance along both path AB and A'B'. For cases using the UDU models, the ε_{eq}^{p} profiles exhibit noticeable heterogeneity. Apart from the observation that ε_{eq}^{p} for a greater $\bar{E}_L$ has a higher peak value in the localised shear band emanating from the crack, it is also noticed that the peak values of ε_{eq}^{p} in the cases using the UDU models are significantly above those obtained using the FLAT model. Thus, we can infer that a larger $\bar{E}_L$ promotes strains and strain localisation in the near-tip region, and as a result will increase the CTOD crack driving force. When $e_{o,avg}$ = 0.035, all pipe models are all well into the globally strain hardening regime, exhibiting nearly constant ε_{eq}^{p} in the locations away from cracked end.

3.3 Crack driving force

The calculated CTOD as a function of average overall strain ($e_{o,avg}$) in the cracked pipe with an average flaw size 5.68×50 mm and 4.41×100 mm is plotted in Fig. 14 and Fig. 15, respectively. The calculated CTOD obtained from the FLAT model and the UDU model with various softening parameters are compared with that measured in the full-scale tests. Clearly, using the FLAT model in the FE analyses for the stationary crack under-predicts the CTOD for $e_{o,avg}$ of above around 0.005. The FE analyses using the UDU models, on the other hand, start to predict a conservative CTOD driving force for strains greater than 0.005. With the UDU models, CTOD increases rapidly initially and reaches a plateau at $e_{o,avg}$ = 0.005. It is evident that increasing $\bar{E}_L$ leads to a higher CTOD plateau with a longer length. The CTOD plateau terminates at different $e_{o,\mathrm{avg}}$ levels, depending on the $\bar{E}_L$ ratios used. The CTOD plateau for each $\bar{E}_L$ value (0.005, 0.015 and 0.025) terminates at an overall average strain $e_{o,avg}$ of 0.0288, 0.0346 and 0.0376, respectively. For the predicted CTOD for flaw size 4.41×100 mm as shown in Fig. 15, significant improvement is observed with the use of UDU material model. In comparison, the Flat model largely under-predicts the CTOD. An increasing gap between the FE and the test results is noticed when $e_{o,avg}$ is above 0.0325. This deviation is due to the assumption in the FE analyses of a stationary crack which neglects crack extension by ductile tearing.

By incorporation of the ductile tearing into the FE model using the mapping approach, the agreement between the FE analyses and the test in the post CTOD plateau regime is significantly improved, as shown in Fig. 15. In the post plateau phase, CTOD obtained using the FLAT model is greater than that calculated using the UDU models. This is because the CTOD predicted using the FLAT model has the shortest plateau, and accordingly the effect of the tearing starts to accumulate earlier than those using the UDU material models. For the cases using the UDU models, the magnitude of the CTOD plateau increases with the increase in $\bar{E}_L$.

3.4 Crack tip plastic zone

To understand the differences in the calculated CTOD with different material models, the plasticity and the stress field near the crack tip were examined. Fig. 18 to Fig. 21 show the contours of the equivalent plastic strain (ε_{eq}^{p}) ahead of the crack tip at the symmetric plane. For $e_{o,avg}$ = 0.002 at which the pipe is globally elastic, a small plastic zone is formed near the crack tip. It is clear that the plastic zone of the FE models simulated with a larger $\bar{E}_L$ exhibits a more localised plastic zone. It is worth noting that ε_{eq}^{p} contours of FE models with $\bar{E}_L = 0.015$ and $\bar{E}_L = 0.025$ are slenderer and more concentrated and branched In Fig. 19 where the plasticity has spread to the bottom of the pipes, no pronounced difference is noticed in the shape of ε_{eq}^{p} contours near the crack tip among all models. It can be noticed that the spread of higher plasticity regime ($\varepsilon_{eq}^{p} \geq 0.02$) is greater using higher $\bar{E}_L$ values. On the other hand, the sizes of ε_{eq}^{p} contours in models using the UDU stress-strain curves remain nearly unchanged. This is because the plastic bands are still propagating and the crack behaviour remains unchanged. However, the crack will start to open further again after the bands have spread throughout the model.

3.5 Crack tip fields

To investigate the crack tip conditions during deformation for different material models, we examined the stress and strain fields near the crack tip. Stress and strain components in the near-tip region were extracted based on a local polar coordinate system originating at the crack tip. Fig. 17 illustrates the position and the stresses/strains orientations defined in the local coordinate system.

Fig. 22 and Fig. 23 show the crack-tip field for strain levels $e_{o,avg} = 0.002$ and $e_{o,avg} = 0.01$, respectively. Only these two strain levels were selected for brevity, as the crack-tip fields for $e_{o,avg} = 0.002$ and $e_{o,avg} = 0.003$, and ones for $e_{o,avg} = 0.01$ and $e_{o,avg} = 0.02$ exhibit similar trends.

For strain $e_{o,avg} = 0.002$, the increase in $\bar{E}_L$ is shown to reduce the nominalised crack opening stress $\sigma_{\theta\theta}$ (Fig. 22 (A)) and the radial stress component σ_{rr} (Fig. 22 (C)) along the crack ligament nearer the crack tip. Similar effect of the $\bar{E}_L$ on the angular distribution of the stress fields (Fig. 22 (B) and Fig. 22 (D)) in the forward sector ahead of the crack tip. The radial distribution of von Mises stress σ_e (Fig. 22 (E)) along the crack ligament also shows a decline nearer the crack tip. A dip is observed at r/δ around 5, especially for UDU model with higher $\bar{E}_L$. This indicates that the Gauss point at that location is undergoing strain softening and Lüders instability. The angular distribution of σ_e (Fig. 22 (F)), on the other hand, exhibit a slight increase in the $\pi/4$ to $\pi/2$ section of the forward sector ahead of the crack tip. Similar trend is observed for the angular distribution of the equivalent plastic strain ε_{eq}^{q} (Fig. 22 (G)). As for the radial distribution of ε_{eq}^{q} along the crack ligament, the values for all material models show nearly no difference.

For strain $e_{o,avg} = 0.01$, the radial distribution of $\sigma_{\theta\theta}$ (Fig. 23 (A)) also show a decrese for higher $\bar{E}_L$, which appears more pronounced in comparison with the Flat model further from the crack tip. Similar trend is observed for the radial distribution of σ_{rr} (Fig. 23(B)). As for the radial distribution of σ_e and ε_{eq}^p along the crack ligament, little differences are observed among those for different material models. This is may be due to that the Lüders instability has propagate to far regions from the near-tip region and the stress state of the near-tip region has been well into the strain hardening regime in which all the stress-strain curves converge.

To understand the effect of the stress-strain model on the stress triaxiality level relevant to ductile fracture, the hydrostatic stress as well as the triaxiality parameter ahead of the crack tip is plotted in Fig. 24 and Fig. 25 for strain levels $e_{o,avg} = 0.002$ and 0.01, respectively. The triaxiality parameter h parameter is defined as:

$$h = \frac{\sigma_h}{\sigma_e} \tag{4}$$

where $\sigma_h = \sigma_{kk}/3$ is hydrostatic or mean stress.

Fig. 24 (A) and Fig. 25 (A) show that in the case using a higher $\bar{E}_L$ value, the hydrostatic near the crack tip is lower. This becomes more prominent when the at a higher global strain ($e_{o,avg}$) level. The stress triaxiality parameter h, however, shows slight increase with increasing $\bar{E}_L$, as shown in Fig. 24 (C) at normalised radial distance around 5. As for the angular distribution, on the other hand, both hydrostatic stress and triaxiality parameters decrease with increasing $\bar{E}_L$ for both strain level $e_{o,avg} = 0.002$ and 0.01. For larger strain ($e_{o,avg} = 0.01$), both hydrostatic stress and triaxiality decrease with increasing $\bar{E}_L$ at normalised radial distance r/δ over 2.

4. Discussion

4.1 Effect of softening modulus on deformation behaviour of cracks in pipes

It is evident from Fig. 14 - Fig. 16 and Fig. 18 - Fig. 21 that the softening modulus (E_L and $\bar{E}_L$) has a pronounced effect on the evolution of plasticity and the crack-tip stress field in the FE model of a cracked pipe, as well as the calculated crack driving force. Softening behaviour, or a negative tangent stiffness ($\partial s/\partial e$) in engineering stress-strain curve, is shown to be necessary to generate Lüders-type strain localisation. Shaw and Kyriakides (1997) also noted this when they were simulating the localisation in NiTi strips loaded in tension. Clearly, the softening modulus ($\bar{E}_L$) plays an important role in the production of Lüders band pattern of the pipe model. To further illustrate the effect of material model on the simulated band pattern, we have captured the images of simulated bands at a certain level of average overall strain ($e_{o,avg}$ = 0.015), as shown in Fig. 26. It can be noticed that with the increase in $\bar{E}_L$, the newly generated strain localisation bands appear sharper and the band width tends to be narrower. The propagating bands at the top edge of the pipe using material models of $\bar{E}_L = 0.015$, and $\bar{E}_L = 0.025$, are of criss-cross or "fish-bone" pattern as reported in literature (Kyriakides et al., 2008; Aguirre et al., 2004; Hallai and Kyriakides, 2011). Using $\bar{E}_L = 0.005$, a diffuse band front can be noticed and is found to propagate from the uncracked end towards the cracked end.

In the studies of bent pipes with Lüders plateau (Aguirre et al., 2004; Kyriakides et al., 2008; Hallai and Kyriakides, 2011), the $\bar{E}_L$ ratio seemed to have marginal influence on the global behaviour (moment-rotation response) when the selected $\bar{E}_L$ sufficed to produce the strain localisation. However, as for the global behaviour of the uni-axial tensile strips, a noticeable difference in the Lüders plateau phase was observed with various $\bar{E}_L$ ratios by others (Wang et al., 2017). It was found that a larger $\bar{E}_L$ led to a higher magnitude of the stress plateau. This finding supports the crack driving force obtained in the present work of a cracked pipe. As a higher stress is predicted at a given strain, the dissipated strain energy is increased, thus leading to higher strain energy release rate and crack driving force at a specified strain. The effect of $\bar{E}_L$ on the crack driving force (in terms of CTOD versus global strain response) seems more prominent than on the global response (force versus global strain response)

Wang et al. (2017) observed noticeable differences in the global behaviour (force-elongation response) in the Lüders plateau phase of uni-axial tensile strips calculated with various $\bar{E}_L$ ratios. They found that larger $\bar{E}_L$ led to higher magnitude of the calculated stress plateau. As for the FE analysis of cracked pipes reported in (Wang et al., 2017) and the present work, the effect of $\bar{E}_L$ on the crack driving force (in terms of CTOD) seems more prominent than on the global response. The influence of the softening modulus on the calculated CTOD is arising from the strain localisation associated with Lüders phenomenon. A larger $\bar{E}_L$ produces a stronger strain localisation which in turn contributes to the crack opening. Besides, a larger softening modulus used in FE analysis predicts a greater decrease in the crack opening stress, and thus implies a larger constraint loss ahead of the crack tip. Therefore, the parameters of UDU stress-strain model, namely the softening modulus (E_L) and Δs, should be carefully selected based on tensile testing programmes to produce suitably conservative results in fracture assessment of cracked components.

4.2 Comparison with existing crack driving force solutions

To assess the state of the art of fracture assessment of cracked pipelines with Lüders plateau and the advantage of using an UDU model in fracture analysis, it is worth performing comparisons between the analysis described in the present study with the existing analytical method for fracture assessment.

Many studies have been conducted to develop methods for strain-based fracture assessment of cracked pipelines. Most of these methods were derived from extensive FE calculations (e.g. Liu et al., 2012; Nourpanah and Taheri, 2010; Chiodo and Ruggieri, 2010; Parise et al., 2015; Østby, 2005)). Others were derived analytically from the original form of reference stress method proposed by Ainsworth (1984) with limited FE validations (e.g Budden, 2006; Budden and Ainsworth, 2012; Smith, 2012; Pisarski et al., 2014; Jia et al., 2016)). Some of these solutions predict the J-integral only, thus the CTOD was calculated by the following relationship:

$$J = m\sigma_0\delta \tag{10}$$

where *m* is a constant that depends on the strain hardening exponent and the configuration of cracked component. Pisarski et al. (2014) reported the value of *m* (equals 1.34) from FE analyses with the rearranged form of Eq.10:

$$m = \frac{J_{\mathrm{FE}}}{\sigma_0\delta_{\mathrm{FE}}} \tag{11}$$

As most of the methods mentioned above are strictly applicable to Ramberg-Osgood (RO) stress-strain models, the RO fit was performed to the measured stress-strain curve that contains Lüders plateau. Two RO fits were obtained, i.e. upper bound and lower bound, depending on which part of the measured curve was used for a best fit, as shown in Fig. 27.

Fig. 28 compares the CTOD versus $e_{o,avg}$ measured from the full-scale test with that calculated by FE using UDU material model with $\bar{E}_L = 0.015$ and that predicted using various existing analytical solutions. All the driving force predictive solutions used in Fig. 28 were originally derived from either FE analyses or theoretical equations that exclusively accounted for stationary cracks. In the range of $e_{o,avg}$ above 0.04, all the predicted CTOD values except that from Smith (2012) are below that measured from the test. This is due to the neglect of crack ductile tearing in these CTOD estimates. The CTOD estimated by using Smith (2012) starts to be above the test result from $e_{o,avg}$ = 0.025. Consequently, it is fair to expect that with the solution by Smith (2012), CTOD would be excessively over-predicted if ductile tearing were included in the analysis. During the CTOD plateau phase, all the analytical solutions under-estimate the CTOD in comparison with the full-scale test. Although the methods from Smith (2012) and DNV-RP-F108 (2006) are based on reference stress concept, the solution by Smith (2012) increases CTOD predicted by DNV-RP-F108 (2006) by about a factor of two, making the CTOD estimate closer to the full-scale test result during the Lüders plateau phase.

The estimates calculated by solutions from Nourpanah and Tehari, Jia, SINTEF, CRES, Parise and Chiodo failed to reproduce the trend of the CTOD as measured in the full-scale test which exhibits a CTOD plateau. Instead, these solutions predict a nearly linearly-rising CTOD with increasing $e_{o,avg}$. The reason for the predicted trend is that these equations were originally derived from FE solutions that used continuously yielding materials, such as Ramberg-Osgood model and simple power-law hardening model, and ignored the Lüders plateau. The solutions by DNV, Smith (2012) and Budden and Ainsworth (2012) capture the trend of the CTOD plateau because these methods allow the use of the actual measured stress-strain curves used in the crack driving force calculations.

In comparison with the analytical solutions, the FE using UDU material model ($\bar{E}_L = 0.015$) predicts suitably conservative CTOD in the range $0.005 \leq e_{o,avg} \leq 0.03$. The FE over-predicts the CTOD by 13% - 47% over the CTOD plateau regime. Because the FE simulated the stationary crack and did not explicitly consider the ductile crack extension (as in Fig. 28), non-conservative CTOD starts to be predicted when $e_{o,avg}$ is above 0.03. Moreover, the gradient of CTOD ($\partial\mathrm{CTOD}/\partial e_{o,avg}$) calculated by FE remains almost constant at $e_{o,avg}$ above 0.035, whereas that measured in the test rose exponentially. The exponential rise in the measured CTOD from the pipe test was caused by the ductile crack extension and strain hardening.

Fig. 29 shows the comparisons of CTOD predicted by various approaches when ductile tearing is incorporated. All predicted the CTOD driving force curves are increased. This increase makes the CTOD predicted using Smith (2012) and Budden and Ainsworth (2012) solutions comparable with the test results in the plateau phase. Excessively over-predicted CTOD can be noticed for most of the solutions at higher strains.

4.3 Use of the UDU material model in fracture assessment of pipes containing crack-like flaws

In the present study, we demonstrated the effectiveness of the UDU material model in FE analysis of cracked pipes with Lüders plateau. The UDU approach requires a series of FE analyses of the uni-axial tensile test to be conducted, and then a comparison is made of the global stress-strain response derived from the FE analysis with the experimentally measured stress-strain curve to fine-tune the softening modulus (E_L and $\bar{E}_L$, and thus Δs). Subsequently, the calibrated UDU stress-strain curve is used in the FE analysis of a flawed structure. An alternative method is to use a sandwich specimen as described by Hallai and Kyriakides (2013). The application of the UDU model in numerical fracture analysis has been shown to effectively capture the strain heterogeneity of a Lüders deforming material and predict a suitably conservative crack driving force is shown to improve the accuracy and reliability of flaw assessment methods.

5. Conclusions

In this study, we conducted a thorough analysis of the fracture responses of a seamless API X65 pipe containing a surface-breaking flaw in a steel which exhibited a Lüders plateau in the tensile stress-strain curve. In using the UDU model to simulate Lüders behaviour, we showed that the softening modulus has a marked effect on the global structural response, Lüders band formation and crack tip stress/strain fields in a cracked pipe. The following conclusions are drawn:

- The stress-strain curves with a flat Lüders stress plateau cannot reproduce the strain localisation in the pipes containing crack-like flaws. On the other hand, the UDU model that includes strain softening is shown to simulate Lüders straining observed in a pipe containing a crack.

- The inclusion of strain softening in the UDU model of the stress-strain curve in the FE analysis predicts a CTOD crack driving force that closely replicates that observed in a full-scale pipe test (when ductile tearing is included in the analysis).

- The crack driving force (CTOD) is sensitive to the softening modulus (E_L) used in FE analyses. Thus, the E_L ratio should be carefully chosen and calibrated through tensile tests to make suitably conservative crack driving force estimates.

- Most of the existing SB-ECA methods neglect the effect of Lüders plateau and thus under-predict the crack driving force.

Acknowledgements

This publication was made possible by the sponsorship and support of TWI and Brunel University London. The work was enabled through, and undertaken at, the National Structural Integrity Research Centre (NSIRC), a postgraduate engineering facility for industry-led research into structural integrity established and managed by TWI through a network of both national and international Universities.

References

Aguirre, F., Kyriakides, S., Yun, H., 2004. Bending of steel tubes with Lüders bands. International Journal of Plasticity 20 (7), 1199 -1225.

Ainsworth, R., 1984. The assessment of defects in structures of strain hardening material. Engineering Fracture Mechanics 19 (4), 633 - 642.

Brocks, W., Scheider, I., 2001. Numerical aspects of the path-dependence of the J-integral in incremental plasticity. Technical Report No. GKSS/WMS/01/08, Geesthacht, Germany.

BS7910:2013+A1:205 Incorporating Corrigenda Nos. 1 and 2, 2015. Guide on methods for assessing the acceptability of flaws in metallic structures. Standard, British Standards Institution.

Budden, P., 2006. Failure assessment diagram methods for strain-based fracture. Engineering Fracture Mechanics 73 (5), 537 - 552.

Budden, P., Ainsworth, R., 2012. The shape of a strain-based failure assessment diagram. International Journal of Pressure Vessels and Piping 89, 59 - 66.

Chiodo, M. S., Ruggieri, C., 2010. J and CTOD estimation procedure for circumferential surface cracks in pipes under bending. Engineering Fracture Mechanics 77 (3), 415 - 436.

Cottrell, A. H., Bilby, B. A., 1949. Dislocation theory of yielding and strain ageing of iron. Proceedings of the Physical Society. Section A 62 (1), 49.

DNV-RP-F108, Jan 2006. Recommended practice DNV-RP-F108: Fracture control for pipeline installation methods introducing cyclic plastic strain. Standard, DET NORSKE VERITAS, Norway.

Fairchild, D., MacIa, M., Kibey, S., Wang, X., Krishnan, V., Bardi, F., Tang, H., Cheng, W., 2011. A multi-tiered procedure for engineering critical assessment of strain-based pipelines. In: Proceedings of the International Offshore and Polar Engineering Conference. pp. 698 - 705.

Hallai, J. F., Kyriakides, S., 2011. On the effect of Lüders bands on the bending of steel tubes. Part II: Analysis. International Journal of Solids and Structures 48 (24), 3285 - 3298.

Hallai, J. F., Kyriakides, S., 2013. Underlying material response for Lüders like instabilities. International Journal of Plasticity 47, 1 - 12.

Hertelé, S., De Waele, W., Denys, R., Verstraete, M., 2012. Justification of the mapping approach for finite element modelling of ductile tearing In: Hertele, S. (Ed.), SUSTAINABLE CONSTRUCTION AND DESIGN.Vol. 3. Ghent University, Laboratory Soete, pp. 36 - 43.

Hertelé, S., ODowd, N., Minnebruggen, K. V., Denys, R., Waele, W. D., 2014. Effects of pipe steel heterogeneity on the tensile strain capacity of a flawed pipeline girth weld. Engineering Fracture Mechanics 115, 172 - 189.

Hutchinson, J., 1968. Singular behaviour at the end of a tensile crack in a hardening material. Journal of the Mechanics and Physics of Solids 16 (1), 676 13 - 31.

Jia, P., Jing, H., Xu, L., Han, Y., Zhao, L., 2016. A modified reference strain method for engineering critical assessment of reeled pipelines. International Journal of Mechanical Sciences 105, 23 - 31.

Johnston, W. G., Gilman, J. J., 1959. Dislocation Velocities, Dislocation Densities, and Plastic Flow in Lithium Fluoride Crystals. Journal of Applied Physics 30 (2), 129 - 144.

Kyriakides, S., Miller, J. E., 2000. On the Propagation of Lüders Bands in Steel Strips. Journal of Applied Mechanics 67, 645.

Kyriakides, S., Ok, A., Corona, E., 2008. Localization and propagation of curvature under pure bending in steel tubes with Lüders bands. International Journal of Solids and Structures 45 (10), 3074 - 3087.

Liu, M., Wang, Y.-Y., Song, Y., Horsley, D., Nanney, S., 2012. Multi-tier tensile strain models for strain-based design part 2 - Development and formulation of tensile strain capacity models. In: Proceedings of the Biennial International Pipeline Conference, IPC. Vol. 4. pp. 415 - 425.

Liu, Y., Kyriakides, S., Hallai, J. F., 2015. Reeling of pipe with Lüders bands. International Journal of Solids and Structures 72, 11 - 25.

Lüders, W., 1860. Über die äusserung der elasticität an stahlartigen eisenstaben und stahlstben, und ber eine beim biegen solcher stäbe beobachtete molecularbewegung. Dinglers Polytech. J. 155, 18 - 22.

Needleman, A., 1988. Material rate dependence and mesh sensitivity in localization problems. Computer Methods in Applied Mechanics and Engineering 67(1), 69 – 85

Nourpanah, N., Taheri, F., 2010. Development of a reference strain approach for assessment of fracture response of reeled pipelines. Engineering Fracture Mechanics 77 (12), 2337 - 2353.

Østby, E., 2005. Fracture control - Offshore pipelines: New strain-based fracture mechanics equations including the effects of biaxial loading, mismatch and misalignment. In: Proceedings of the International Conference on Offshore Mechanics and Arctic Engineering - OMAE. Vol. 3. pp. 649 - 658.

Parise, L., Ruggieri, C., O'Dowd, N., 2015. Fully-Plastic Strain-Based J Estimation Scheme for Circumferential Surface Cracks in Pipes Subjected to Reeling. Journal of Pressure Vessel Technology, Transactions of the ASME 137 (4).

Piobert, G., Morin, A. J., Didion, I., 1842. Commission des principes du tir. Memorial de lartillerie 5, 501 - 552.

Pisarski, H., Smith, S., London, T., 2014. Flaw tolerance of pipelines containing circumferential flaws subjected to axial straining and internal pressure tests and analyses. International Journal of Offshore and Polar Engineering 24 (3), 199 - 205.

R6 Rev.4, 2001. Assessment of the integrity of structures containing defects. Standard, EDF Energy, Gloucester, UK.

Rice, J., Rosengren, G., 1968. Plane strain deformation near a crack tip in a power-law hardening material. Journal of the Mechanics and Physics of Solids 16 (1), 1 - 12.

Rice, J. R., 1968. A Path Independent Integral and the Approximate Analysis of Strain Concentration by Notches and Cracks. Journal of Applied Mechanics 35 (2), 379 - 386.

Shaw, J., Kyriakides, S., 1997. Initiation and propagation of localized deformation in elasto-plastic strips under uniaxial tension. International Journal of Plasticity 13 (10), 837 - 871.

Shih, C., 1981. Relationships between the J-integral and the crack opening displacement for stationary and extending cracks. Journal of the Mechanics and Physics of Solids 29 (4), 305 - 326.

Smith, S., 2012. Development of the BS 7910 failure assessment diagram for strain based design with application to pipelines. In: Proceedings of the International Conference on Offshore Mechanics and Arctic Engineering - OMAE. Vol. 3. pp. 431 - 436.

Tang, H., Fairchild, D., Panico, M., Crapps, J., Cheng, W., 2014. Strain Capacity Prediction of Strain-Based Pipelines. In: 2014 10th International Pipeline Conference. American Society of Mechanical Engineers, pp.V004T11A025 - V004T11A025.

Tkaczyk, T., O'Dowd, N. P., Nikbin, K., Howard, B. P., 2009. A non-linear fracture assessment procedure for pipeline materials with a yield plateau. In: Proceedings of the 19th International Offshore and Polar Engineering Conference. pp. 100 - 109.

Wang, L., Eren, E., Wang, B., Wu, G., July 2017. Consideration of yield discontinuity in the elastic-plastic fracture analysis of circumferentially flawed pipes. In: Proceedings of ASME 2017 Pressure Vessels and Piping Conference. Vol. 6A: Materials and Fabrication. American Society of Mechanical Engineers, Waikoloa, Hawaii, USA, p. V06AT06A035.

Tables

Table 1 Parameters of material models used in FE analyses of cracked pipes

Material No.	E (GPa)	R_{eL} (MPa)	$\Delta e_L\%$	$\bar{E}_L$	$\Delta s/R_{eL}$
FLAT	210	512	2.0	0	0
UDU 1				0.005	0.041
UDU 2				0.015	0.122
UDU 3				0.025	0.203

Figures

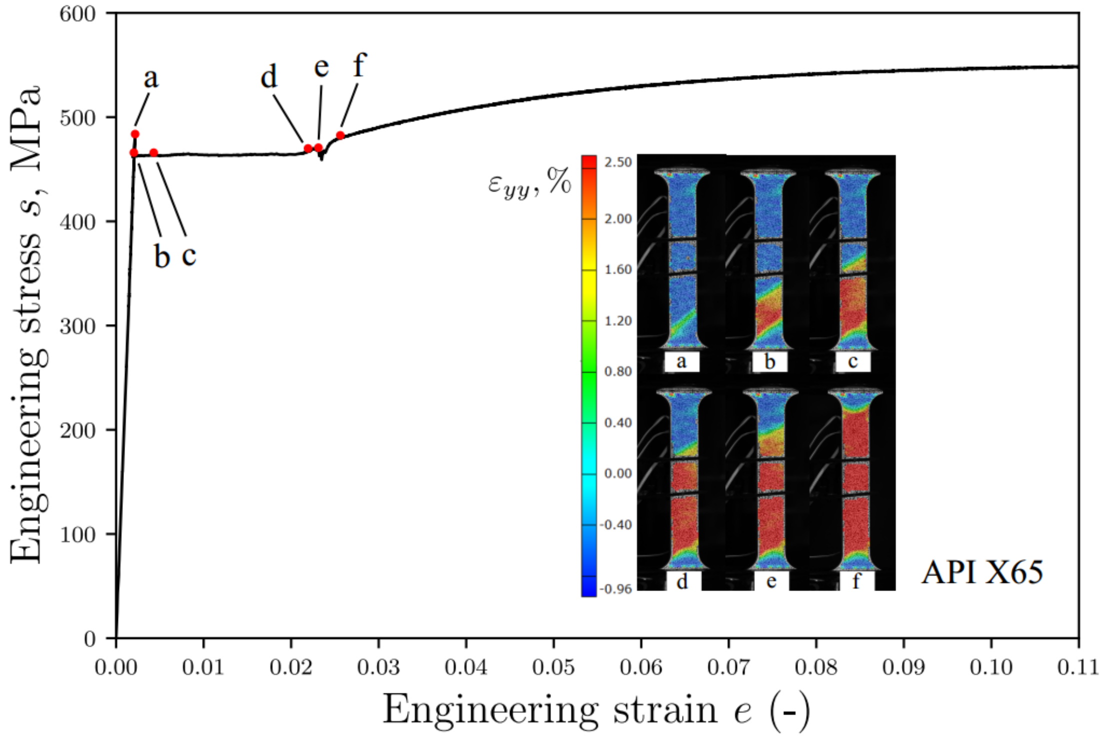

Fig. 1 Stress-strain response of a typical X65 strip exhibiting a Lüders plateau

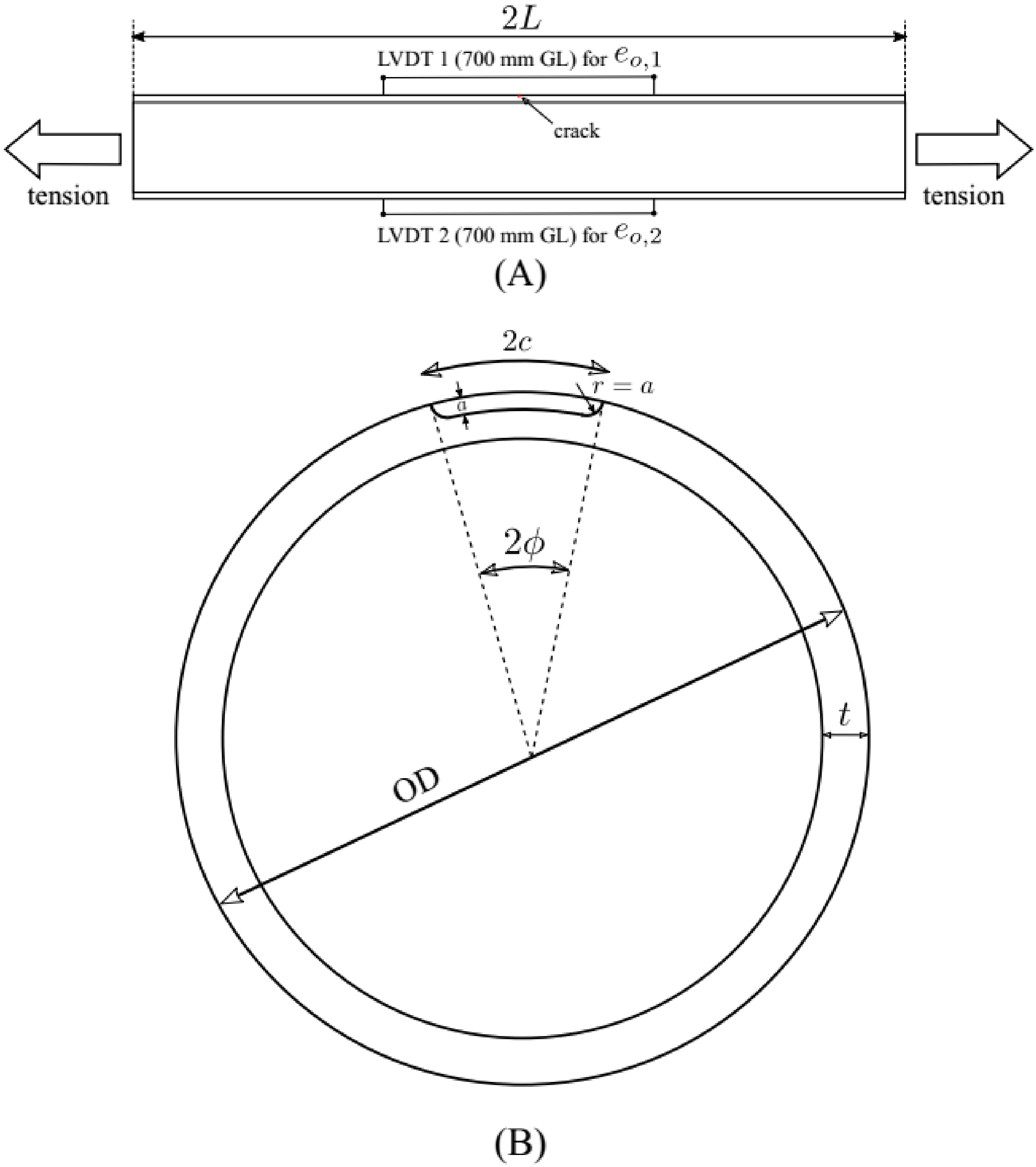

Fig. 2 Schematic of the pipe containing a surface-braking flaw: (A) geometric features of the pipe in the longitudinal view; (B) geometric features of the pipe cross-section containing an external surface-breaking flaw

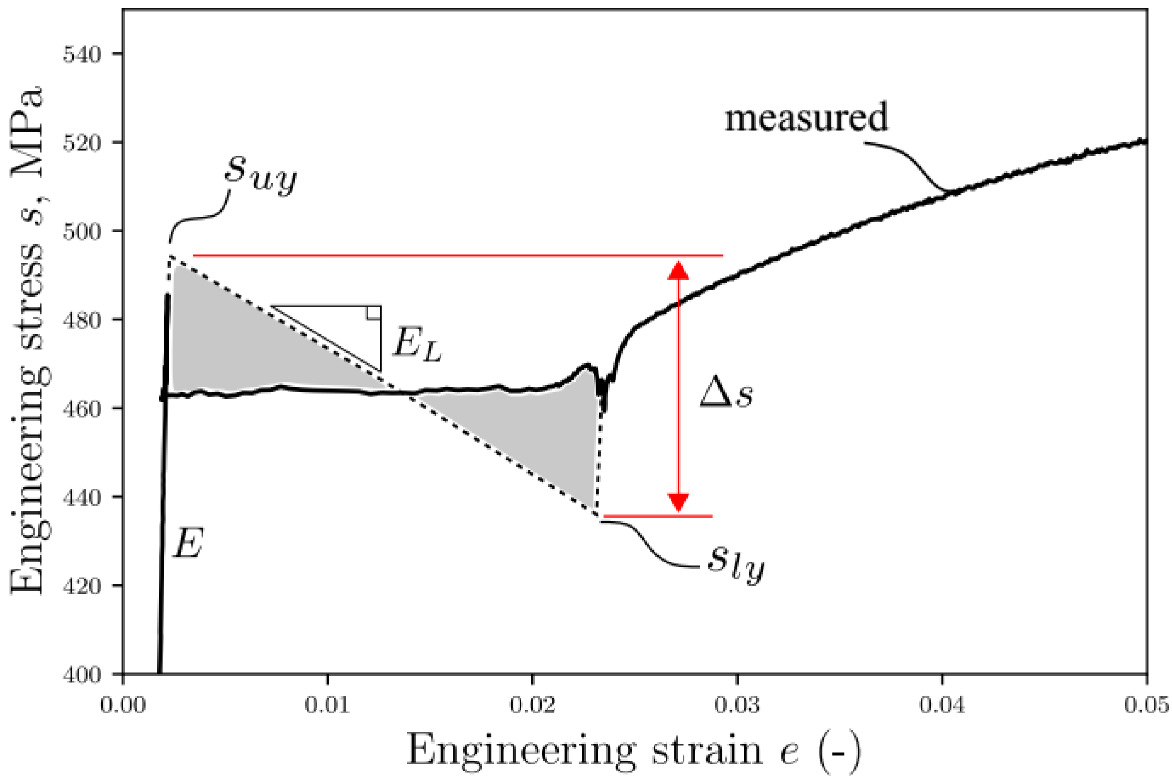

Fig. 3 Illustrative schematic of up-down-up (UDU) stress-strain model

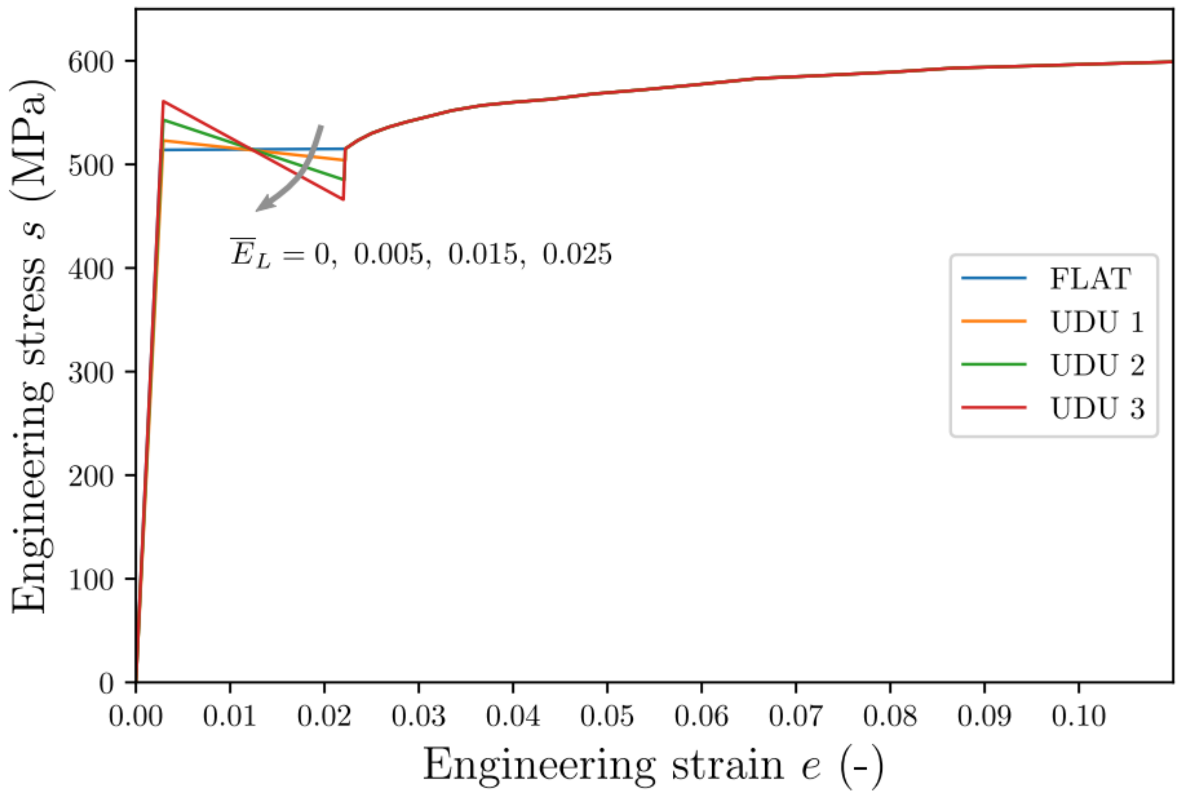

Fig. 4 Constitutive models used in FE analyses

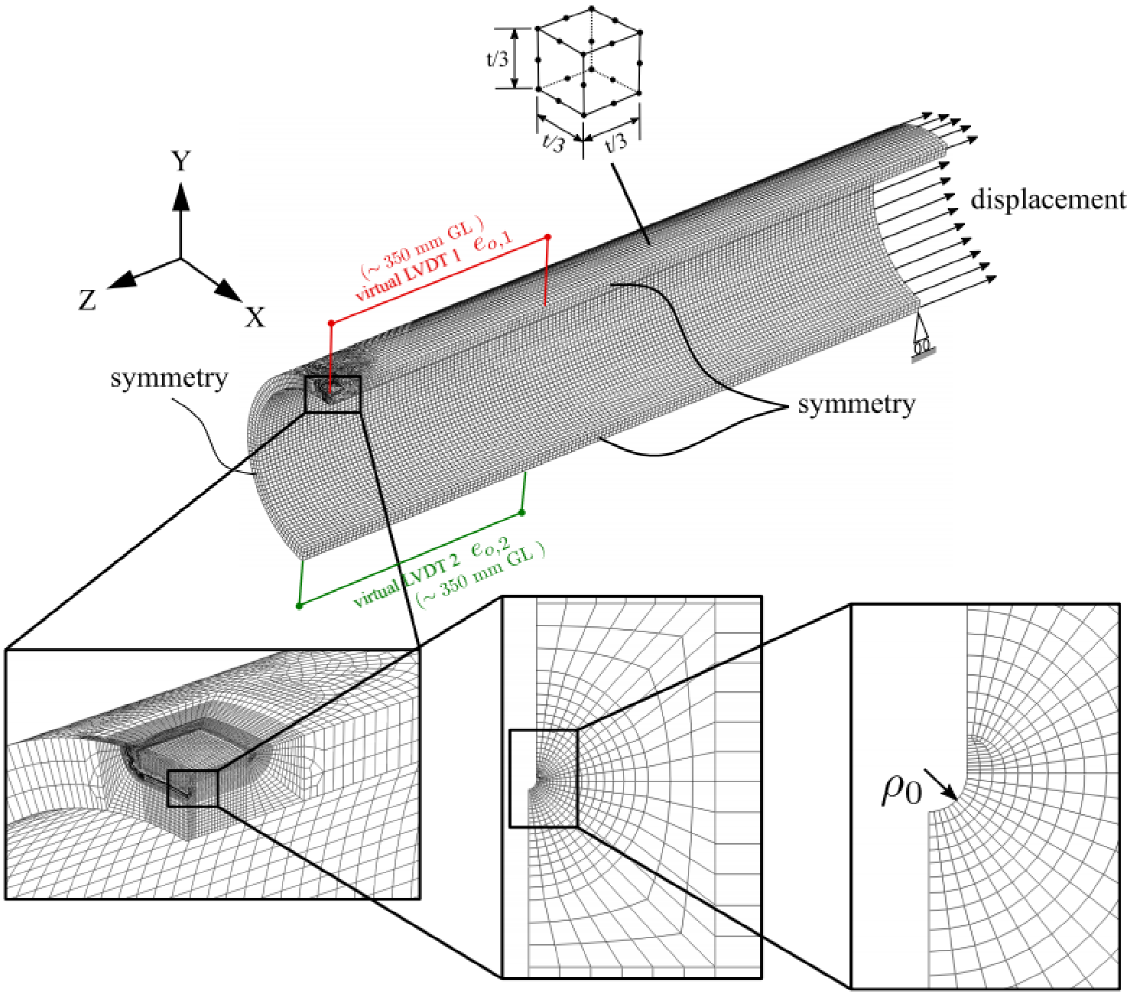

Fig. 5 Mesh configuration of the cracked pipe FE model

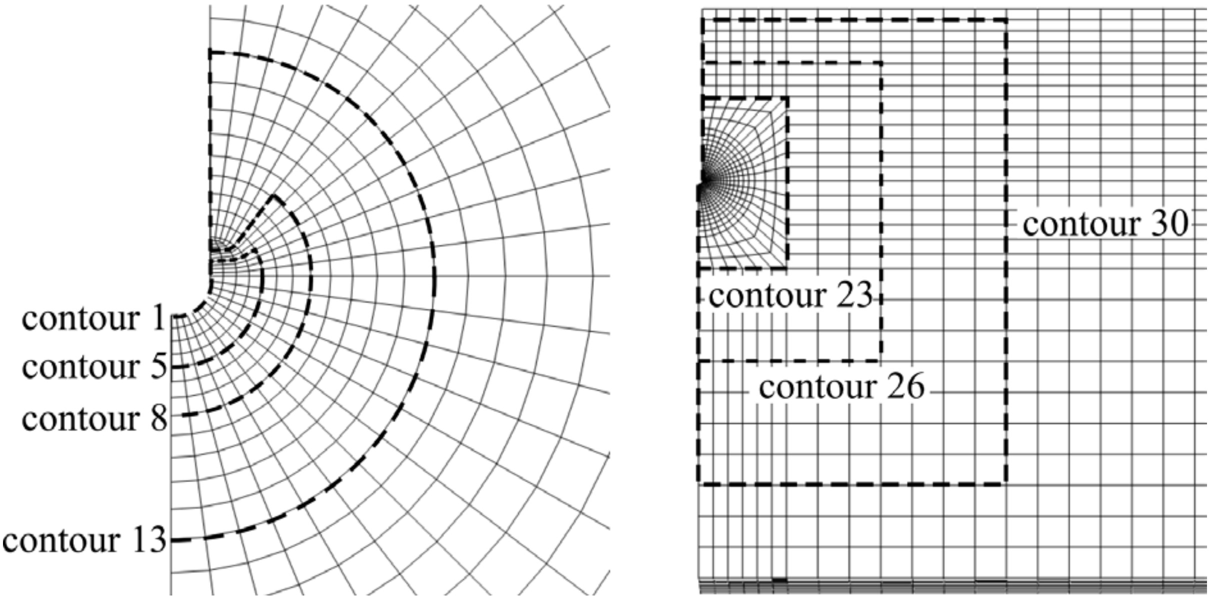

Fig. 6 Crack-tip and near-tip regions showing the contours from which J values were extracted

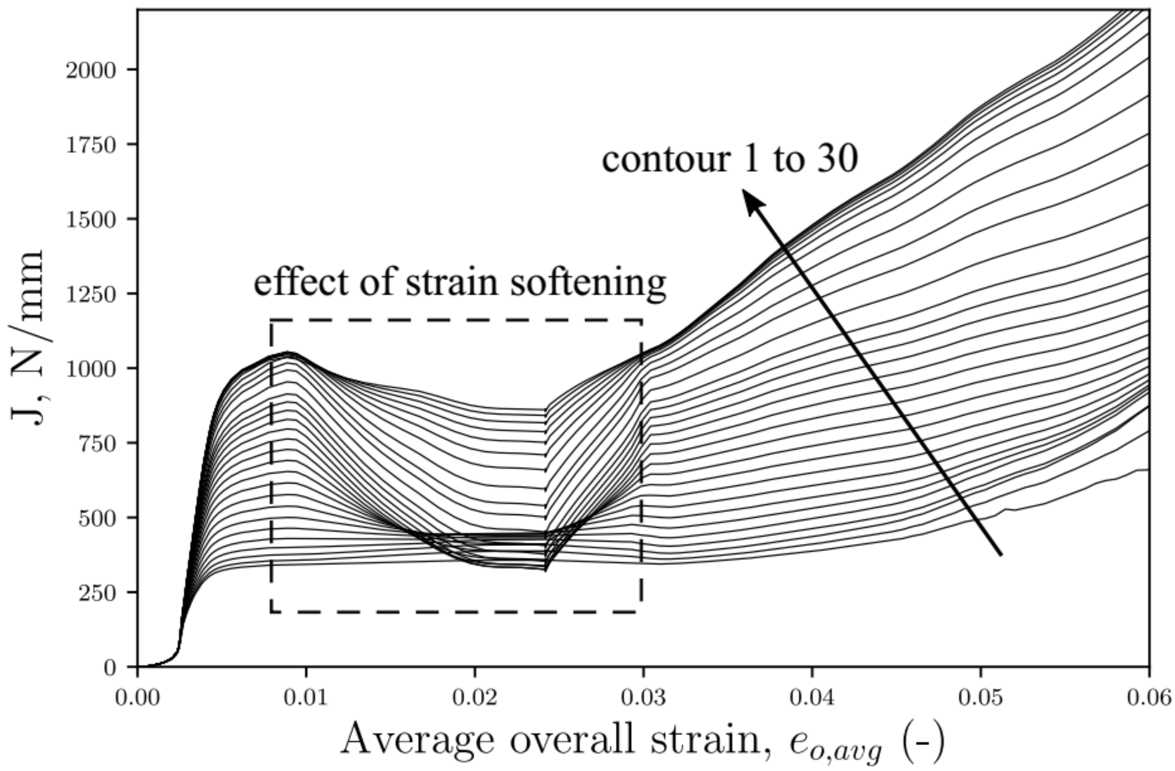

Fig. 7 Calculated J-integral of cracked pipes for UDU model with $\bar{E}_L = 0.005$

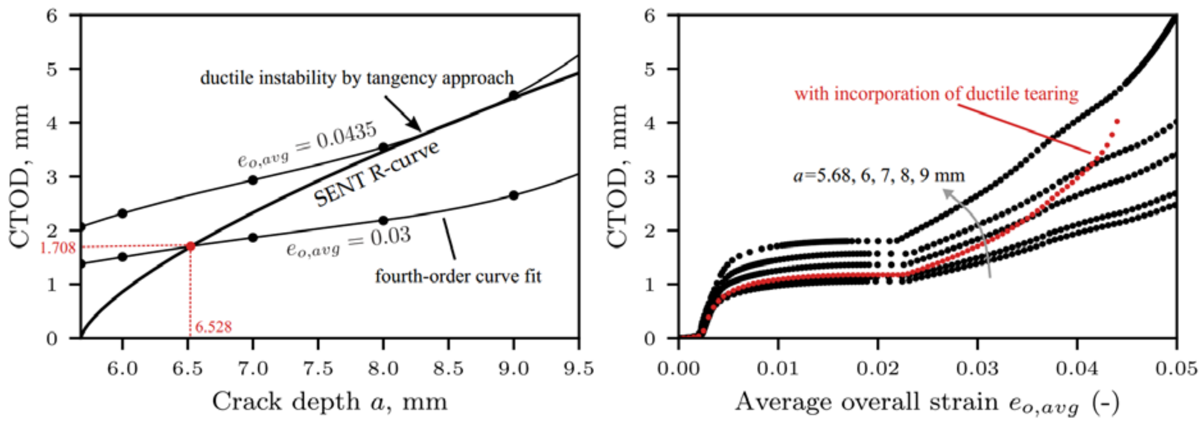

Fig. 8 Incorporation of ductile tearing by driving force mapping and tangency approach

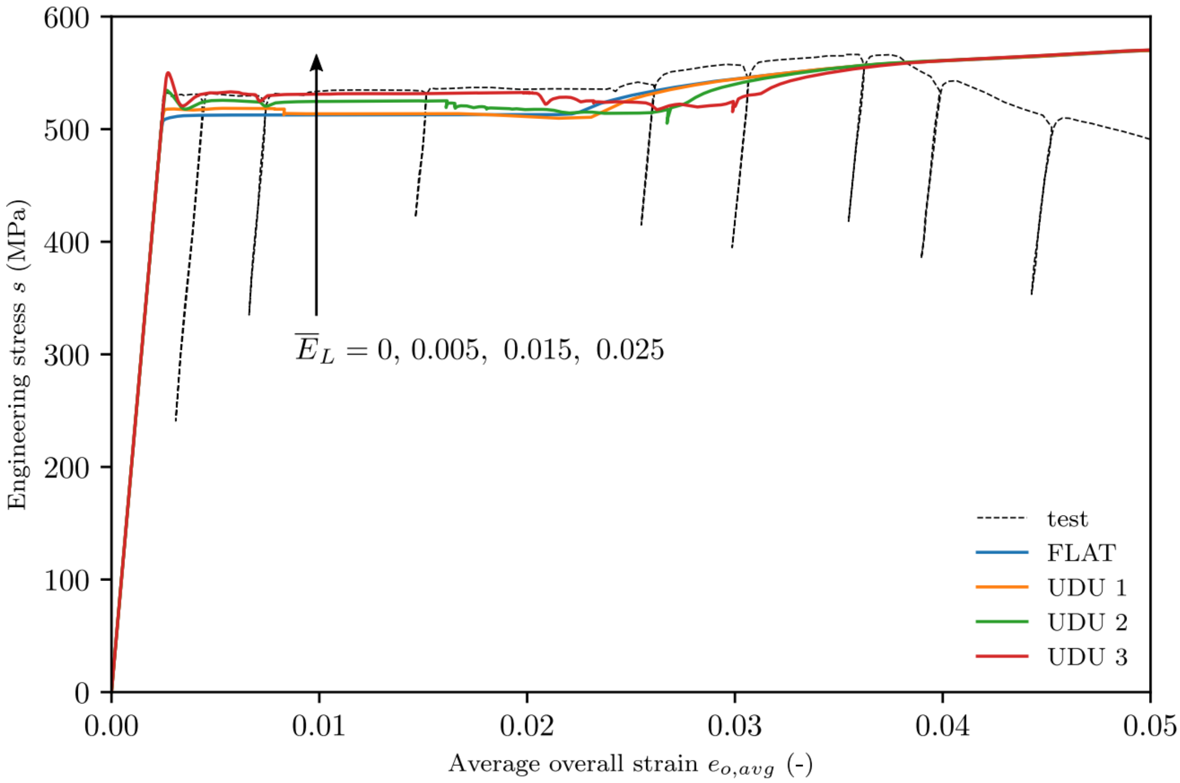

Fig. 9 Comparison of global response from FE analyses and TWI full-scale test

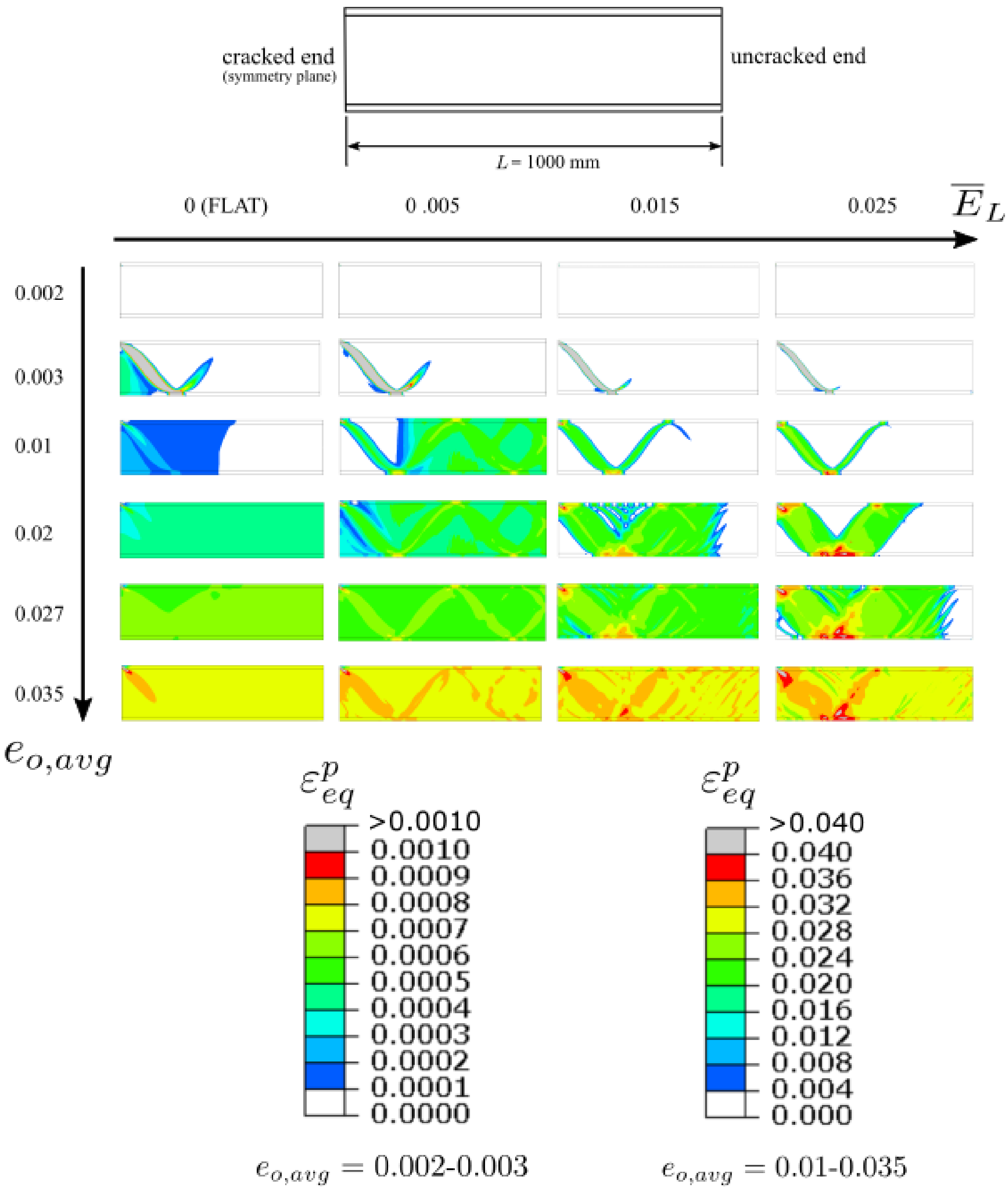

Fig. 10 Equivalent plastic strain (ε_eq^p) contours of the simulated cracked pipe with different material models at certain average overall strains $e_{o,avg}$

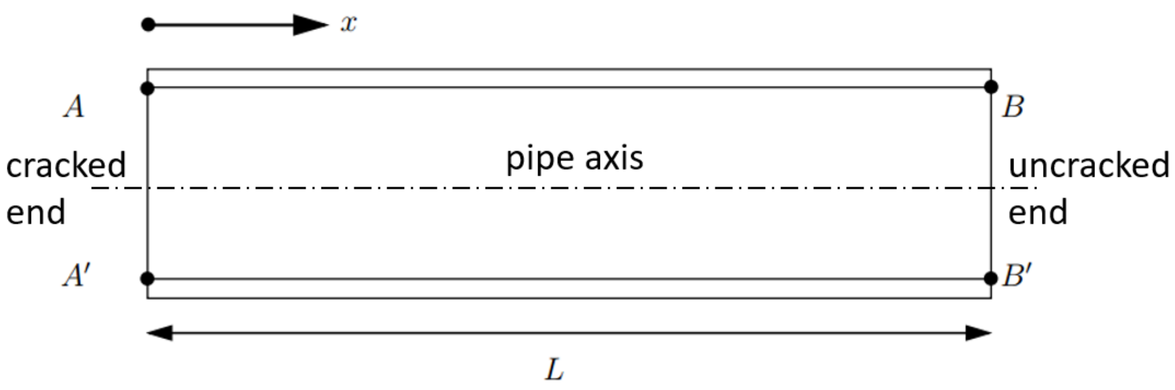

Fig. 11 Paths AB and A'B' selected to extract equivalent plastic strain ε_{eq}^{p} *profiles*

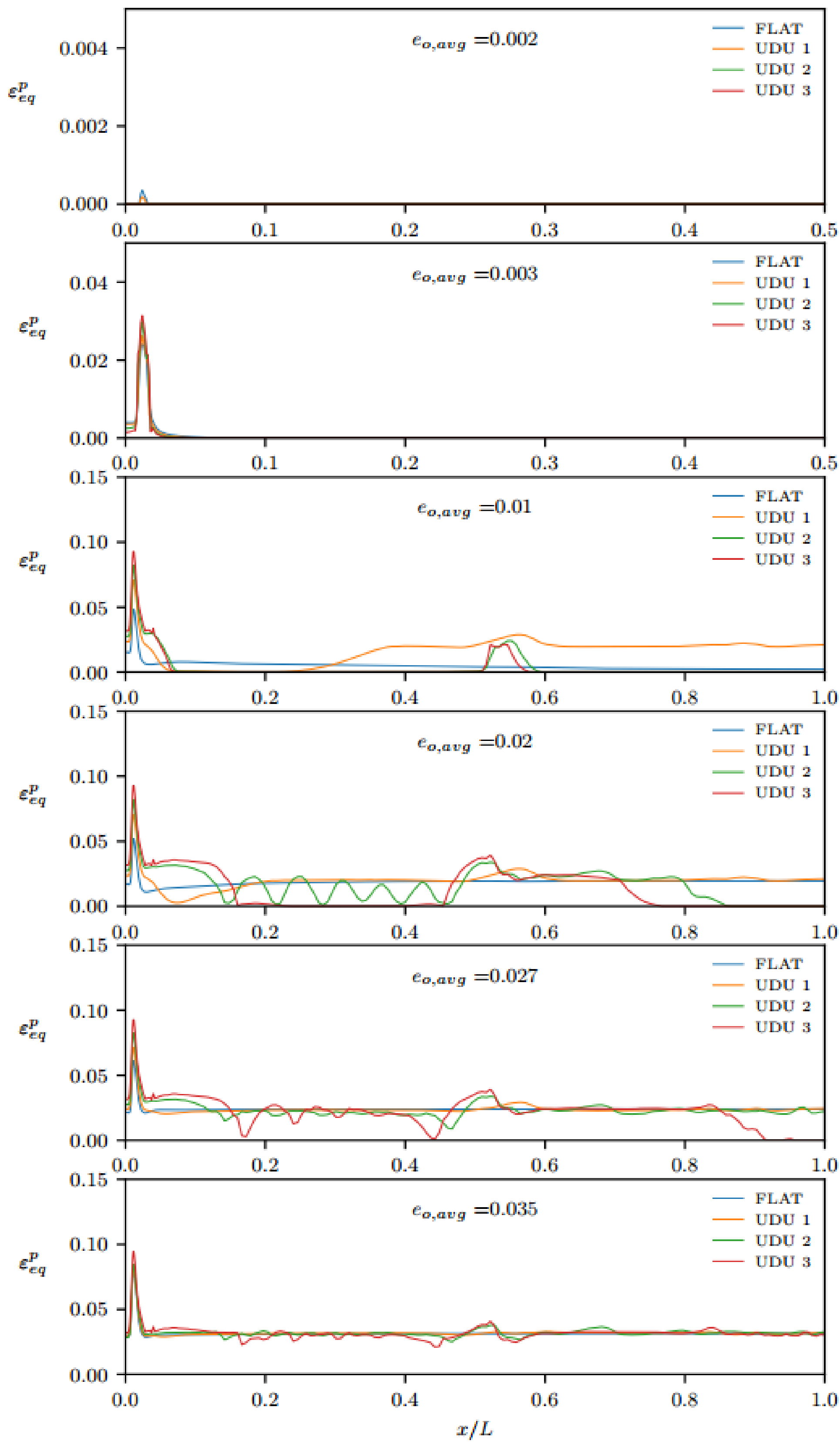

Fig. 12 Equivalent plastic strain ε^p_{eq} profile along path AB

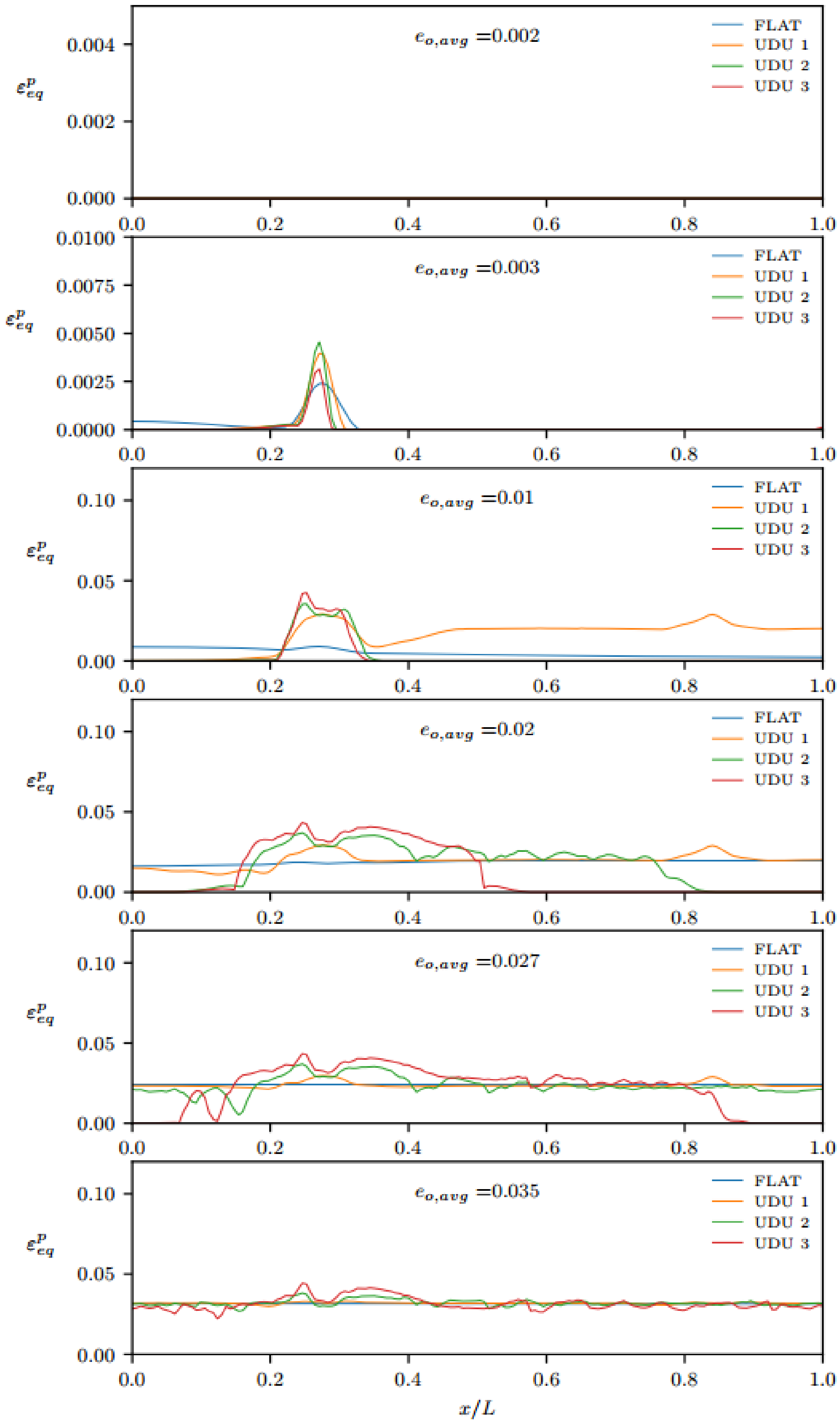

Fig. 13 Equivalent plastic strain ε^p_{eq} profile along path A'B'

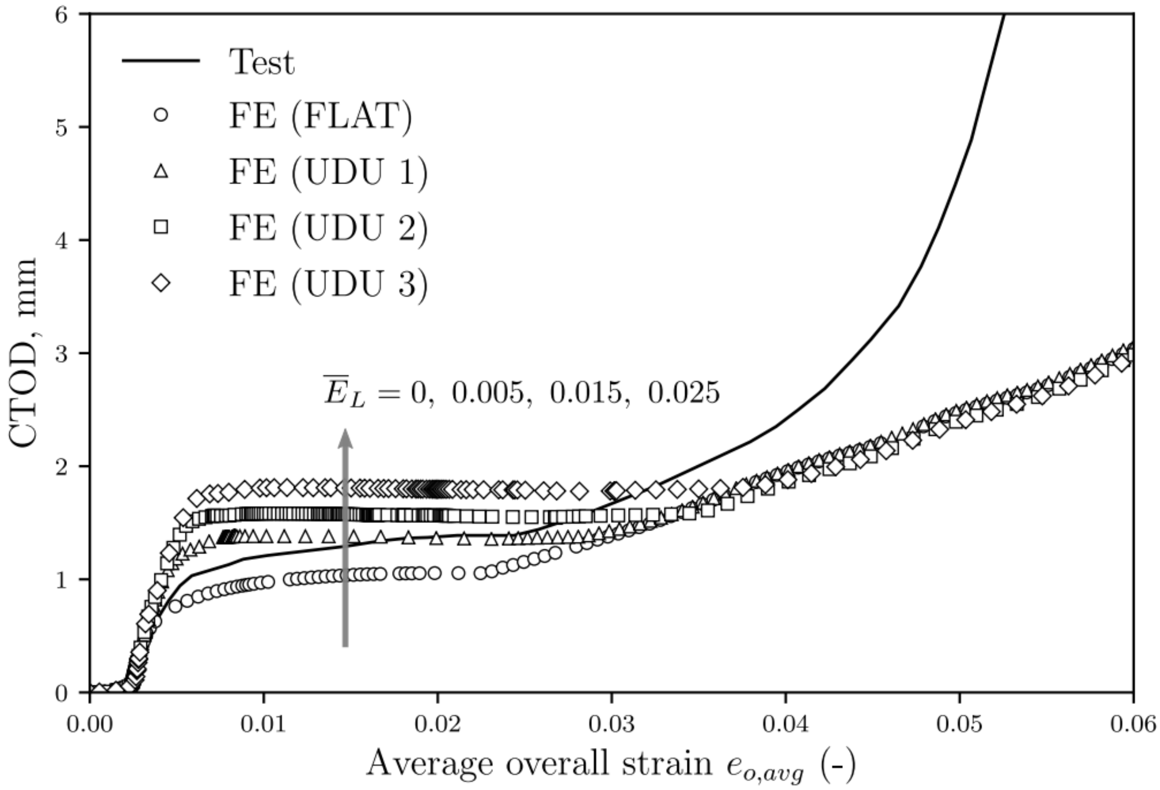

Fig. 14 Comparison of CTOD for average crack size 5.68 x 50 mm from test and FE analyses without consideration ductile

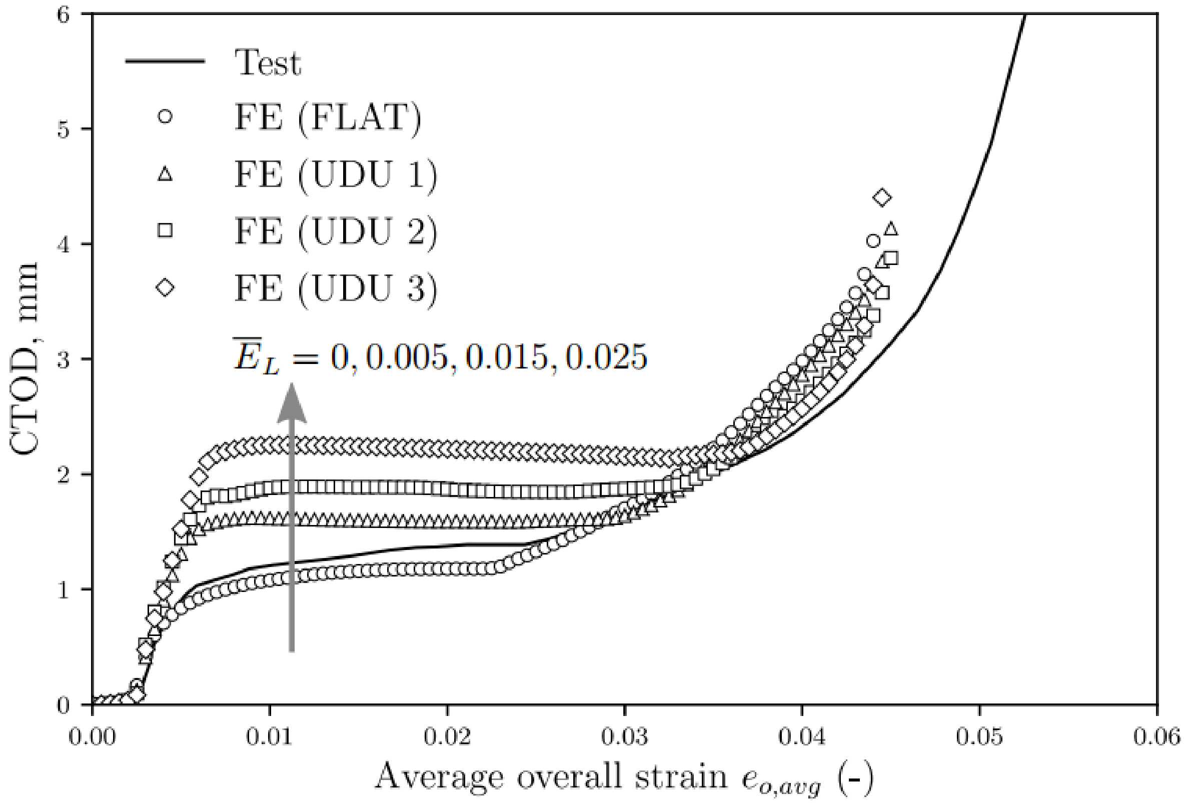

Fig. 15 Comparison of CTOD for average crack size 5.68×50 mm from test and FE analyses with consideration of ductile tearing

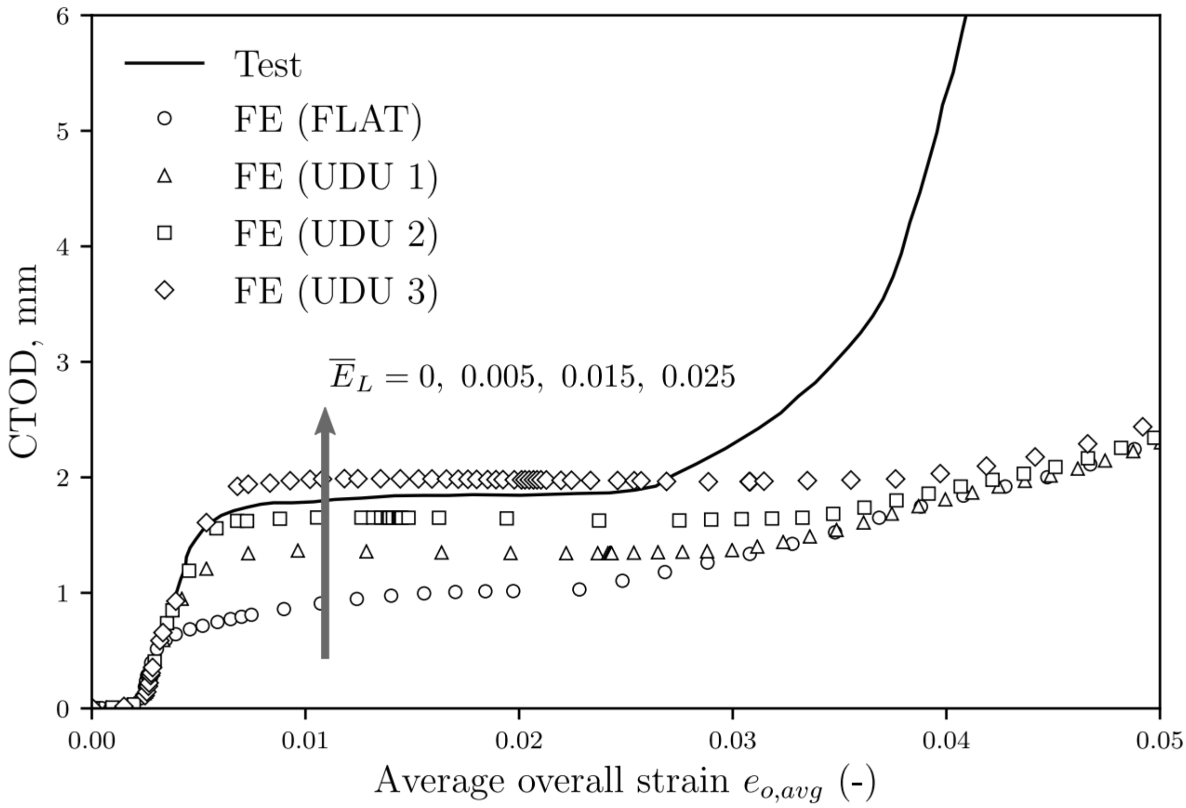

Fig. 16 Comparison of CTOD for average crack size 4.6×100 mm from test and FE analyses without consideration ductile

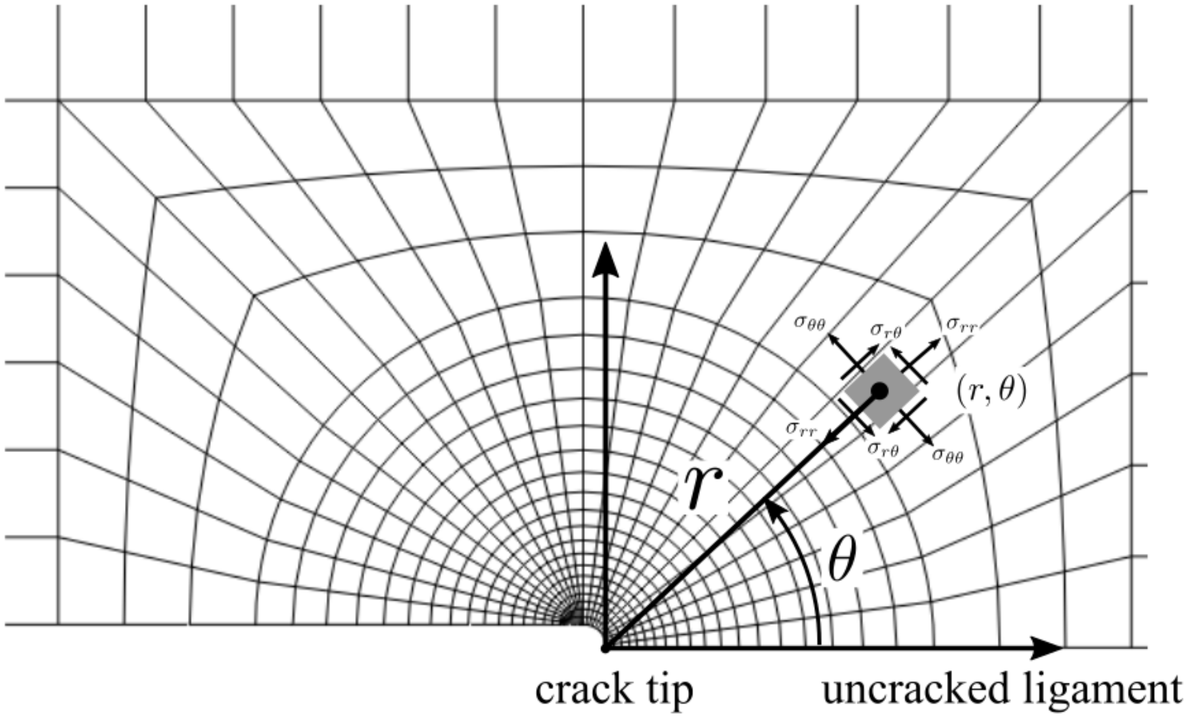

Fig. 17 Local coordinates defined ahead of the crack tip

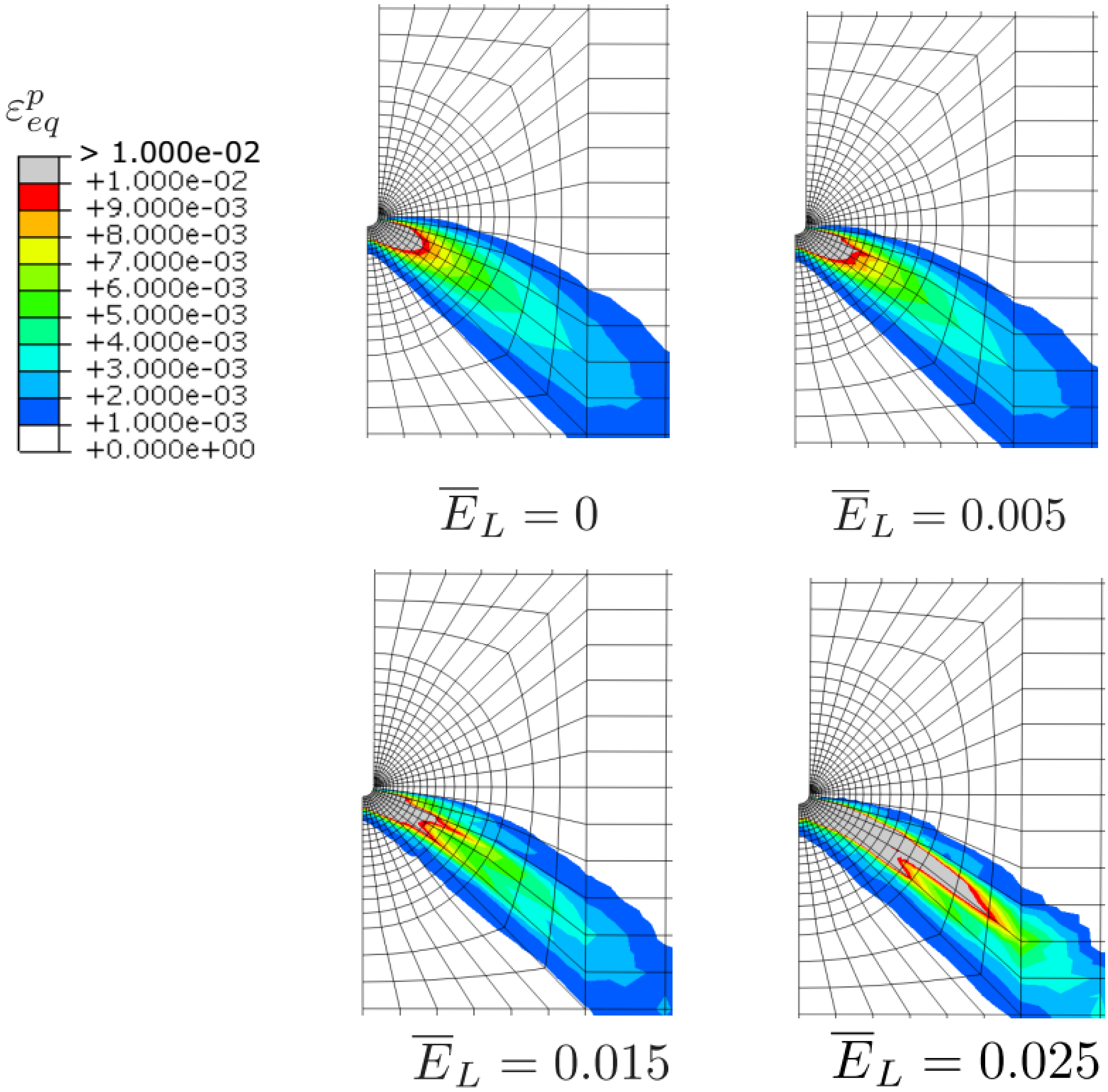

Fig. 18 Equivalent plastic strain ε^p_{eq} contours in near-tip region at $e_{o,avg} \approx 0.002$ from FE analyses using different material models

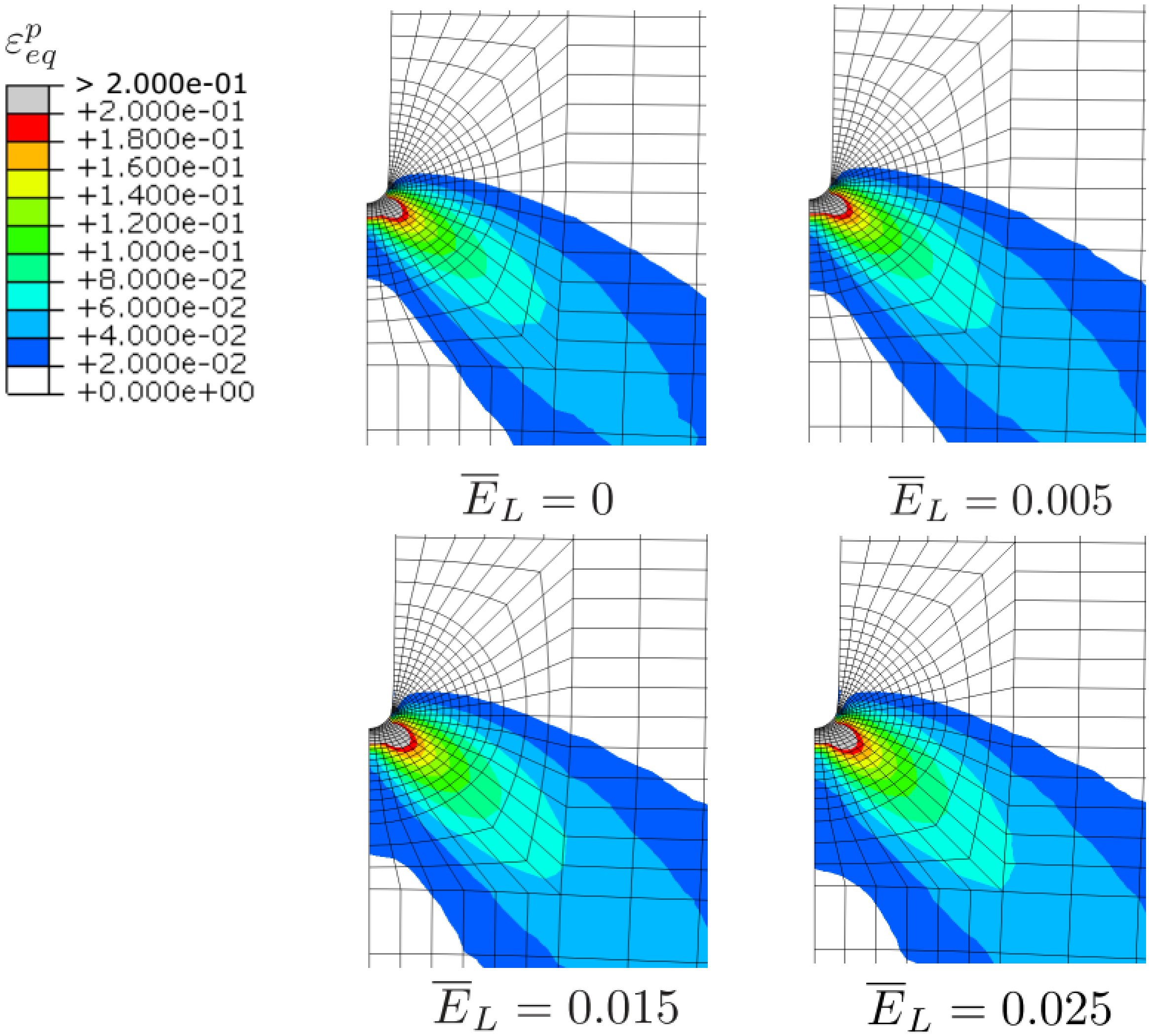

Fig. 19 Equivalent plastic strain ε^p_{eq} contours in near-tip region at $e_{o,avg} \approx 0.003$ from FE analyses using different material models

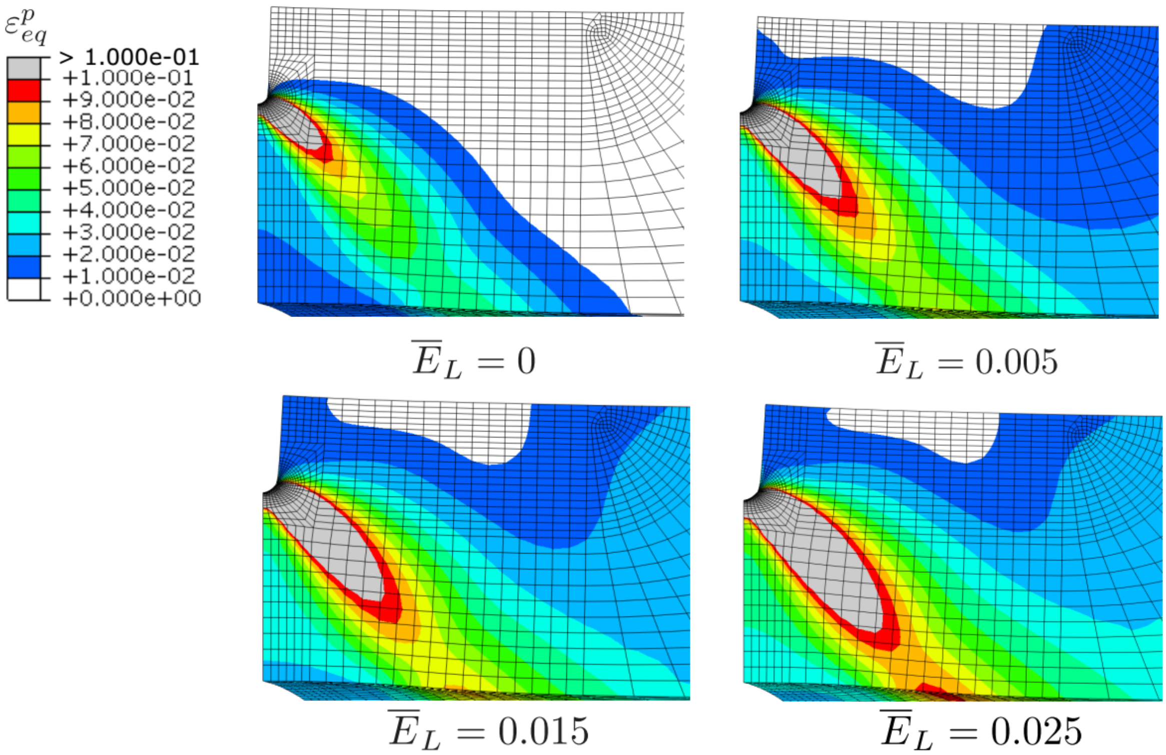

Fig. 20 Equivalent plastic strain ε_{eq}^{p} contours in near-tip region at $e_{o,avg} \approx 0.01$ from FE analyses using different material models

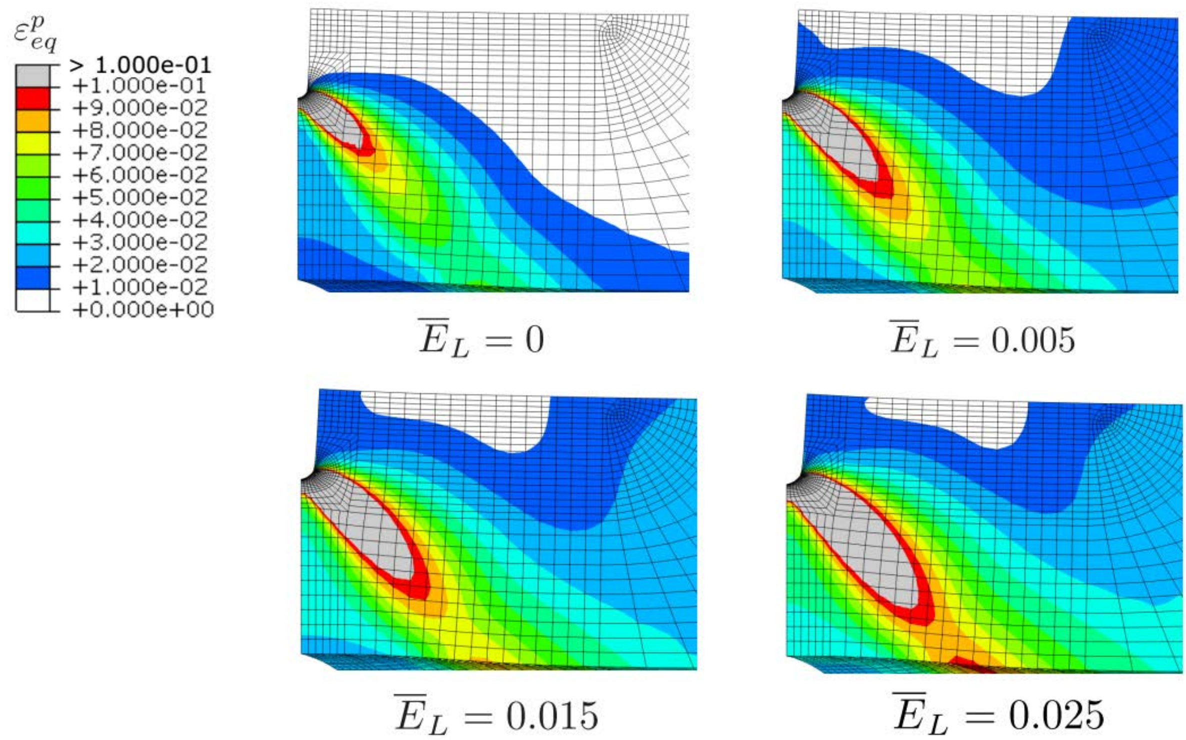

Fig. 21 Equivalent plastic strain ε_{eq}^{p} contours in near-tip region at $e_{o,avg} \approx 0.02$ from FE analyses using different material models

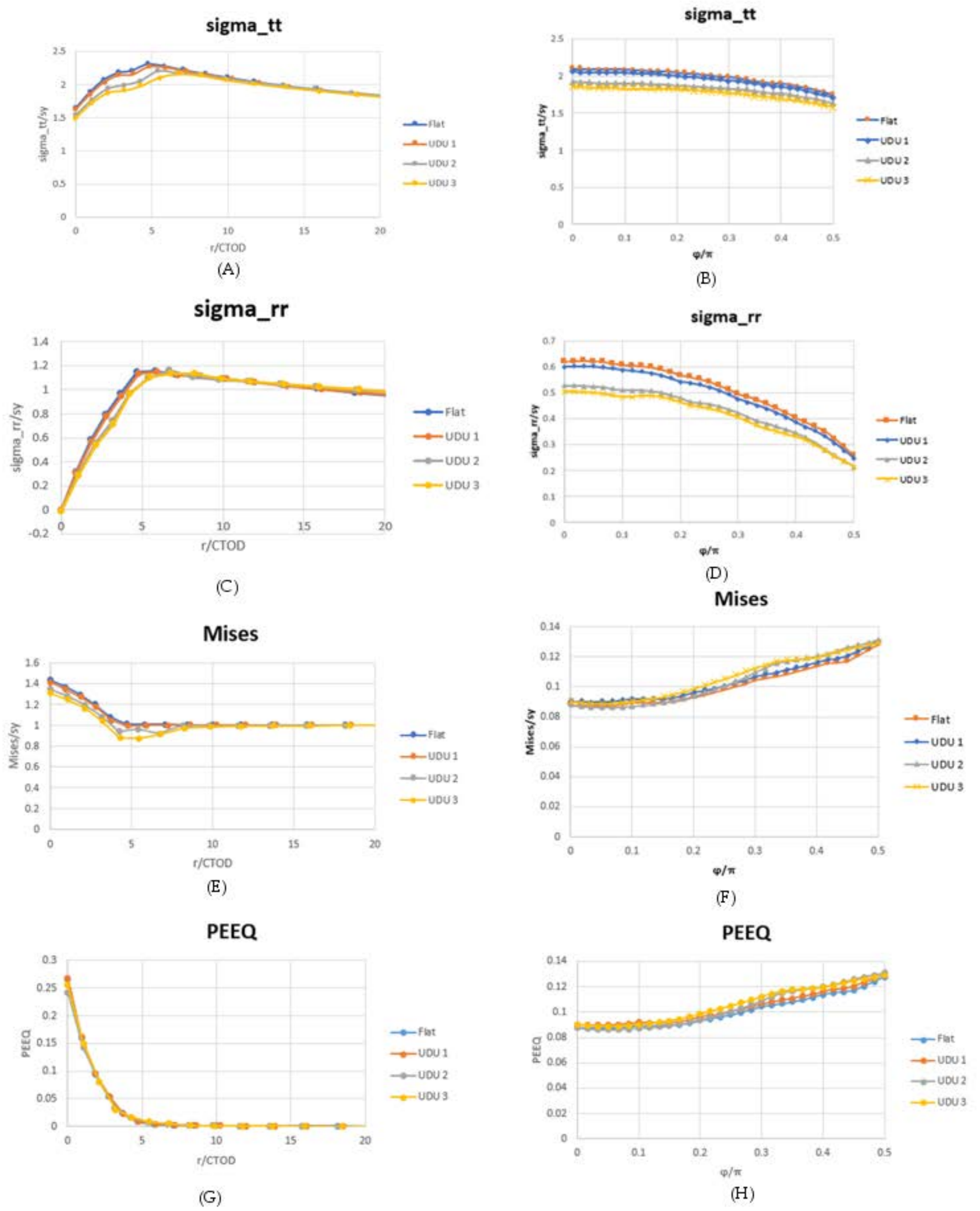

Fig. 22 Crack-tip field at average overall strain level $e_{o,avg} = 0.002$*: radial distribution of tangential stress component* $\sigma_{\theta\theta}$ *(A), radial stress component* σ_{rr} *(C), von Mises effective stress* σ_e *(E) and hydrostatic stress (G) at angle* $\theta = 0$ *; angular distribution of tangential stress component* $\sigma_{\theta\theta}$ *(B), radial stress component* σ_{rr} *(F), von Mises effective stress* σ_e *(F) and hydrostatic stress (H) at normalised radial distance* $r/\delta = 2$

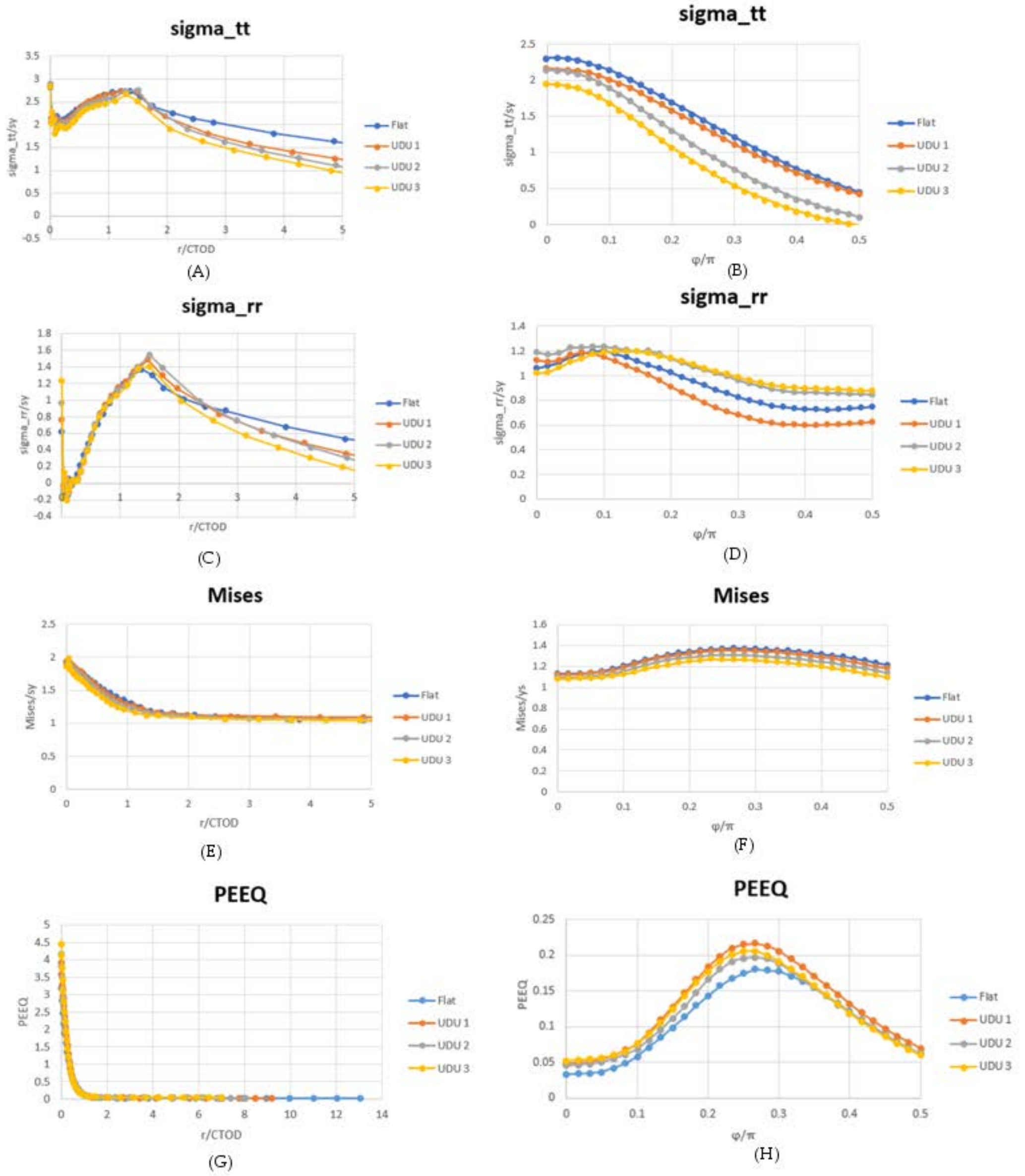

Fig. 23 Crack-tip field at average overall strain level $e_{o,avg} = 0.01$: radial distribution of tangential stress component $\sigma_{\theta\theta}$ (A), radial stress component σ_{rr} (C), von Mises effective stress σ_e (E) and hydrostatic stress (G) at angle $\theta = 0$; angular distribution of tangential stress component $\sigma_{\theta\theta}$ (B), radial stress component σ_{rr} (F), von Mises effective stress σ_e (F) and hydrostatic stress (H) at normalised radial distance $r/\delta = 2$

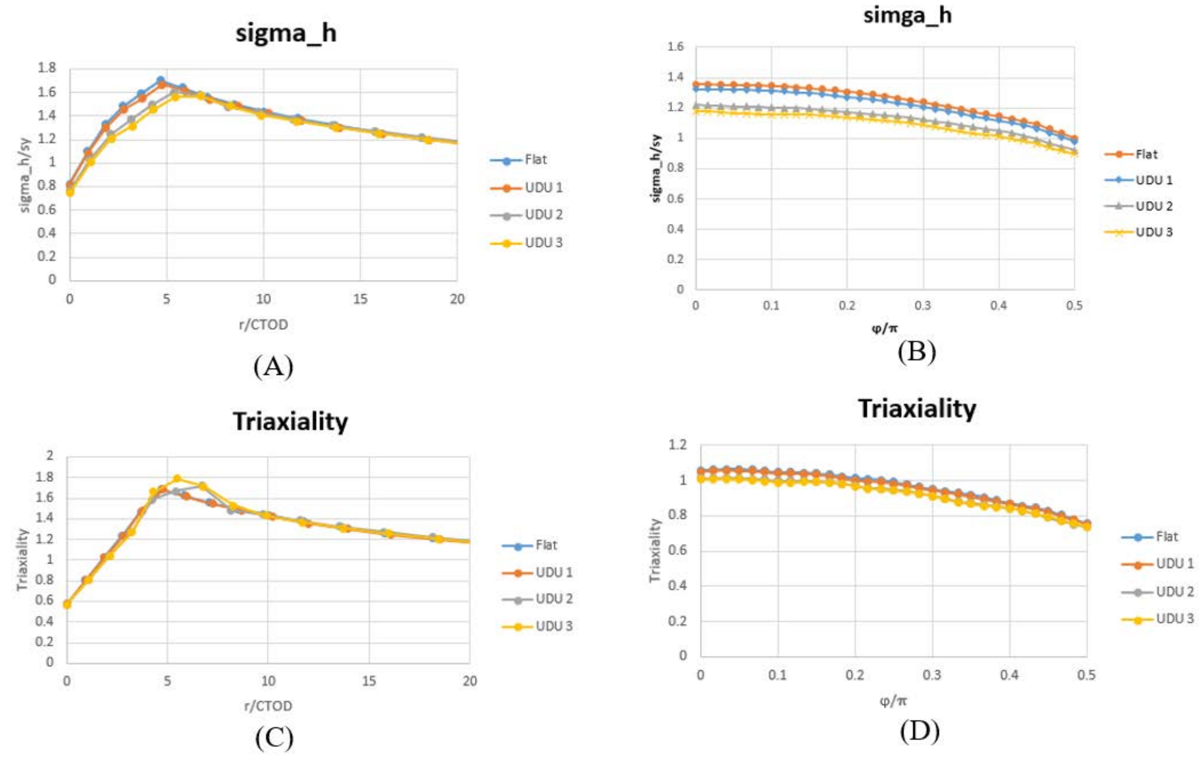

Fig. 24 Crack-tip field at average overall strain level $e_{o,avg} = 0.002$: radial distribution of hydrostatic stress (A), triaxiality parameter (C); angular distribution of hydrostatic stress (B), triaxiality parameter at normalised radial distance $r/\delta = 2$

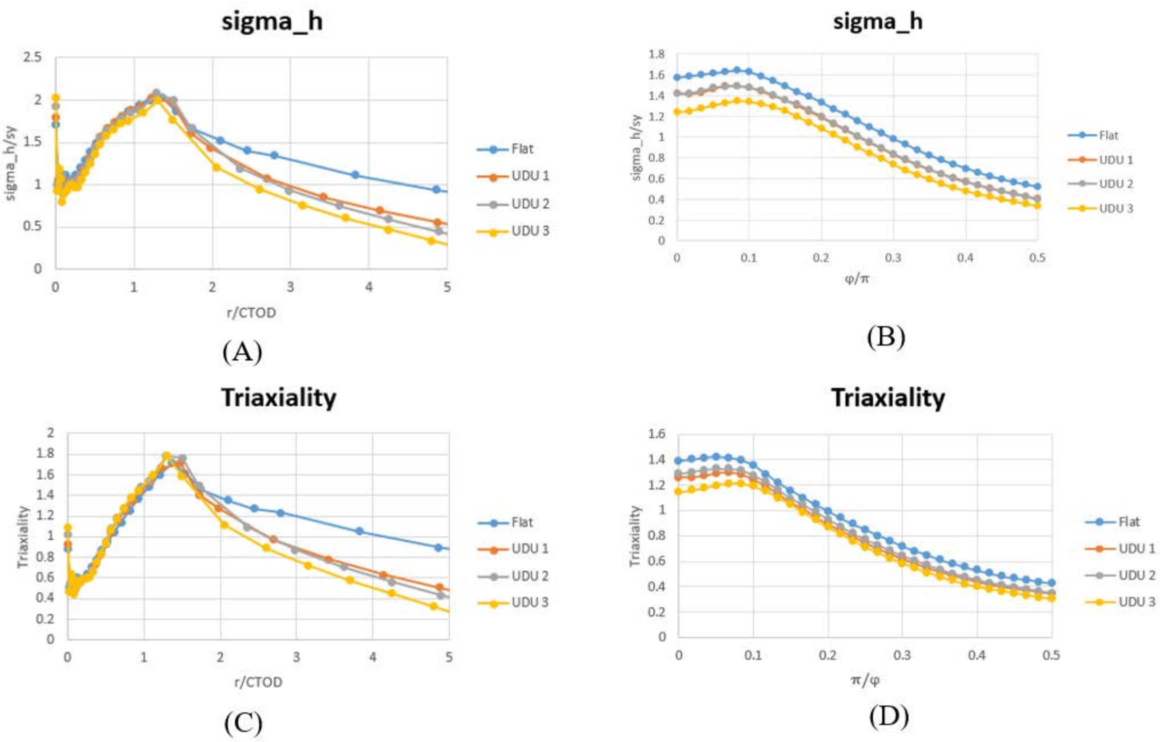

Fig. 25 Crack-tip field at average overall strain level $e_{o,avg} = 0.01$: radial distribution of hydrostatic stress (A), triaxiality parameter (C); angular distribution of hydrostatic stress (B), triaxiality parameter at normalised radial distance $r/\delta = 2$

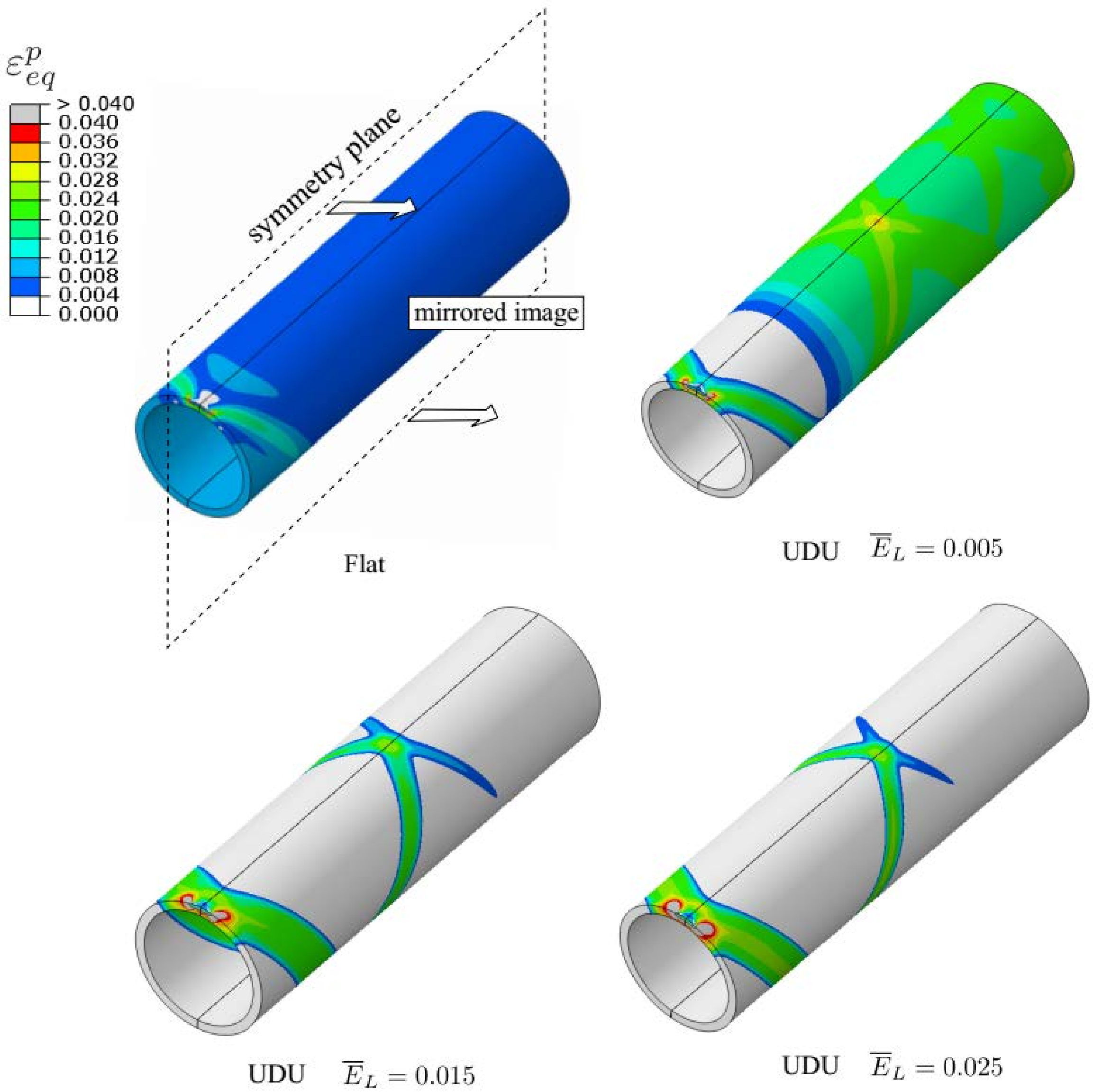

Fig. 26 Lüders band pattern simulated with different material models at average overall strain $e_{o,avg} = 0.015$

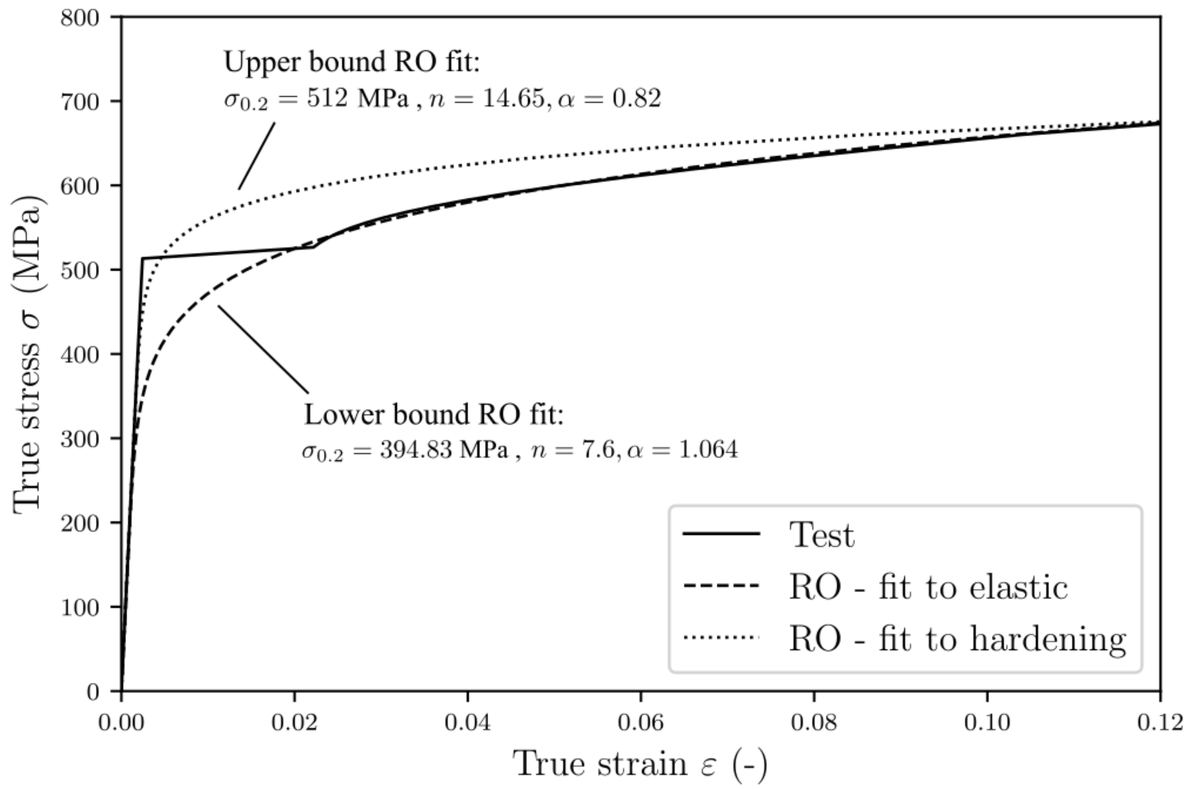

Fig. 27 RO fit to the measured stress-strain (true stress-true strain neglecting the upper yield stress) curve of the pipe material

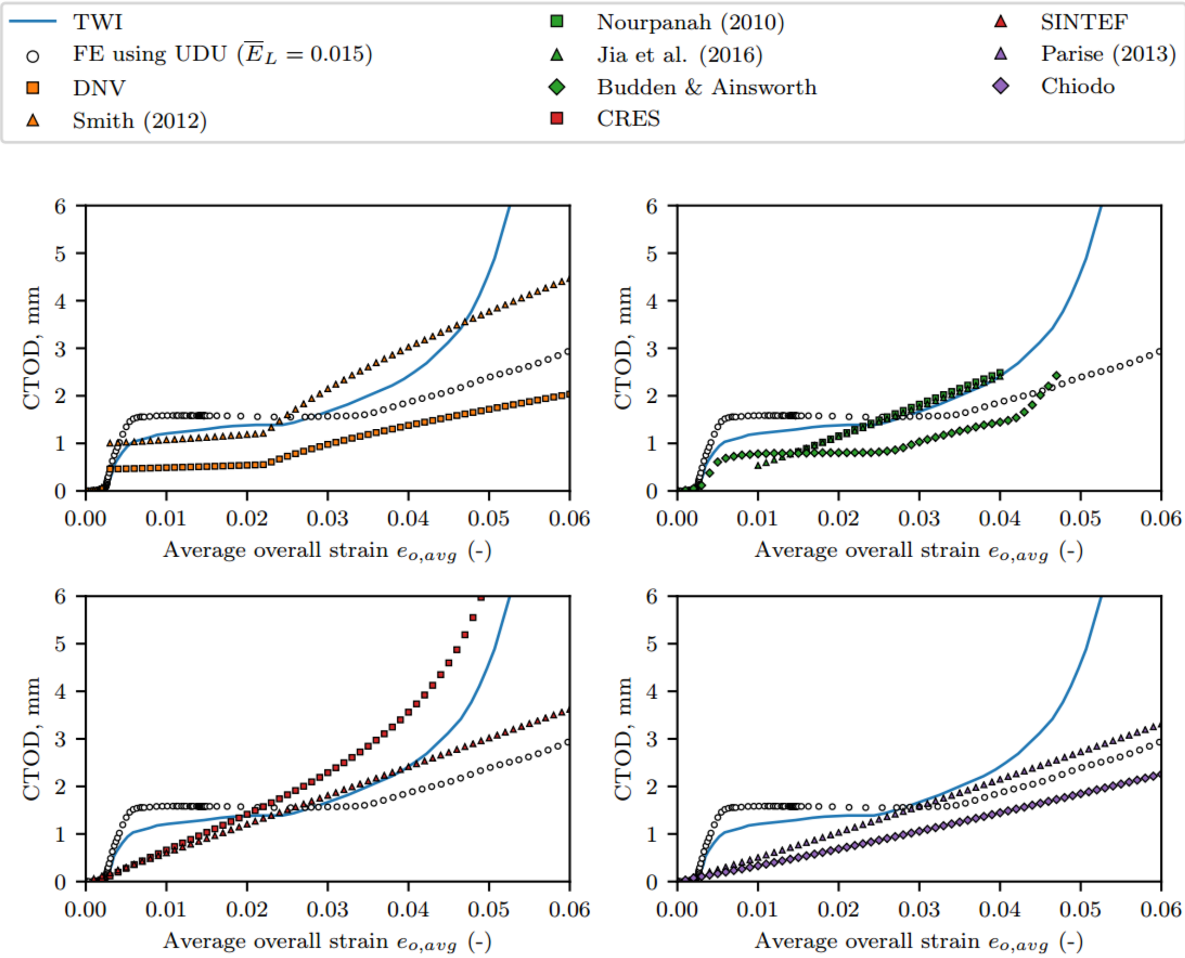

Fig. 28 Comparison of CTOD for nominal crack size 5×60 mm from full-scale test, FEA and analytical solutions (without consideration of ductile tearing)

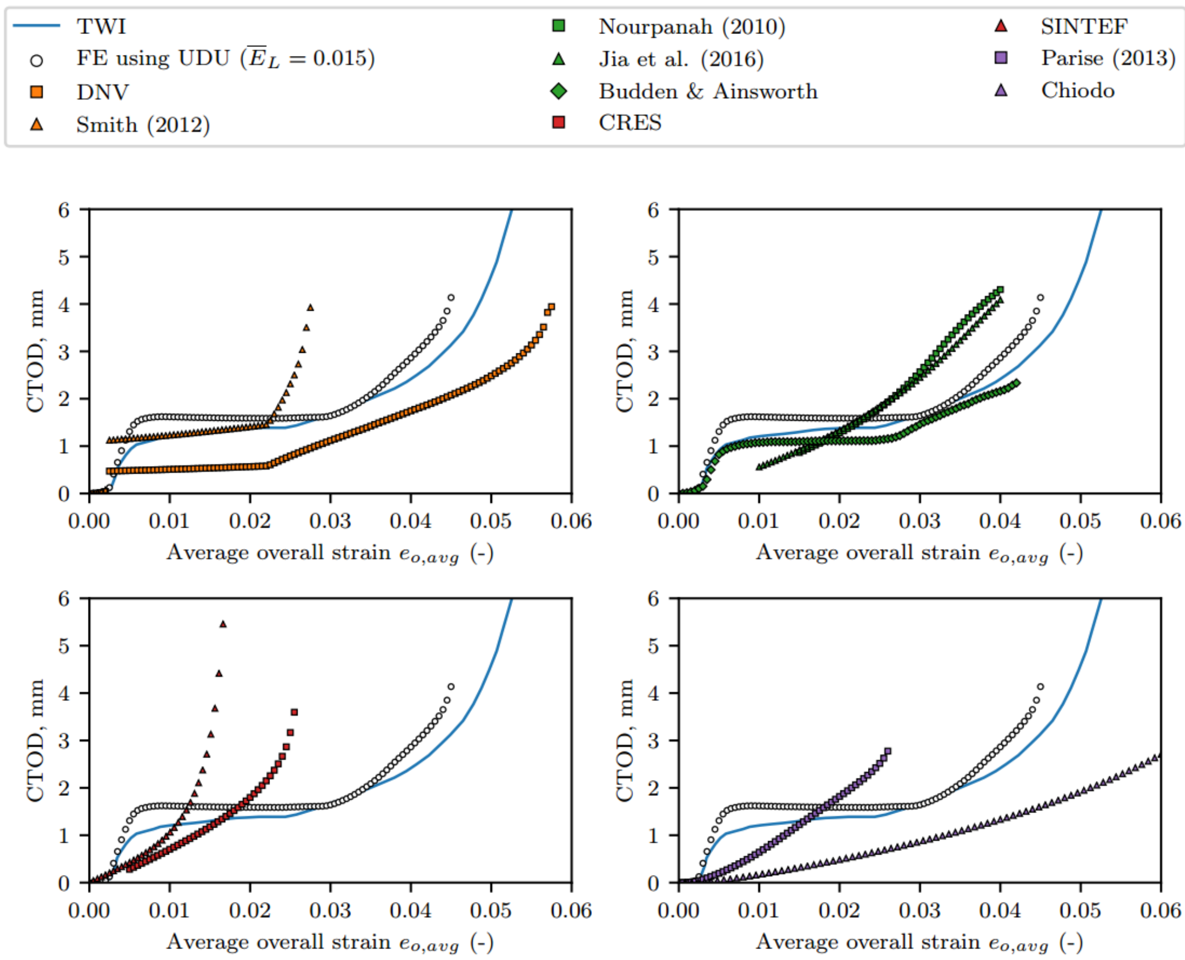

Fig. 29 Comparison of CTOD from full-scale test, FEA and analytical solutions (with consideration of ductile tearing)